minerals

MDPI

Article

Genetic and Sealing Mechanisms of Calcareous Sandstones in the Paleogene Zhuhai–Enping Formations, Panyu A Sag, Pearl River Mouth Basin

Yong Zhou [1,*], Guangrong Peng [2], Wenchi Zhang [2], Xinwei Qiu [2], Zhensheng Li [2], Ke Wang [1], Xiaoming Que [2] and Peimeng Jia [2]

[1] College of Geosciences, China University of Petroleum, Beijing 102249, China; wangke253@163.com
[2] Shenzhen Branch of CNOOC (China) Limited, Shenzhen 518082, China; penggr@163.com (G.P.); wczhang2025@126.com (W.Z.); qiuxinw@126.com (X.Q.); lizhs@163.com (Z.L.); quexiaom@126.com (X.Q.); jpeimeng@126.com (P.J.)
* Correspondence: zhouyong@cup.edu.cn

Abstract

Calcareous sandstones, acting as sealing layers, play a crucial role in hydrocarbon accumulation of formations with high sand content (sand content > 80%). However, the genetic mechanisms, sealing mechanisms, and effectiveness of calcareous sandstones remain unclear. This study takes the Zhuhai–Enping formations in the Panyu A Sag as an example. By comprehensively analyzing data from well logs, cores, cast thin sections, elemental geochemical analysis and carbon–oxygen isotopes, the genetic mechanisms, development patterns, and controlling effects on hydrocarbon accumulation of calcareous cement layers are investigated. The main findings are as follows: (1) The calcareous sandstone cements are mainly composed of dolomite, ankerite, and anhydrite. With increasing burial depth, dolomite transitions from micritic dolomite to silt-sized and fine-crystalline dolomite, and finally to coarse-crystalline dolomite. (2) The local transgression provided ions such as Ca^{2+} and Mg^{2+}, forming the material basis for early dolomite formation. As burial depth increased, the diagenetic environment shifted from acidic to alkaline, leading to the dolomitization of early-formed calcite and the formation of ankerite. (3) The high source-reservoir displacement pressure difference effectively seals hydrocarbon accumulation. Vertically interbedded tight calcareous sandstones and thin marine transgressive mud-stones collectively control efficient hydrocarbon preservation and enrichment. This research addresses the current limits in the study of "self-sealing sandstone layers," and provides new geological insights and predictive models for hydrocarbon exploration in sand-rich settings.

Keywords: calcareous sandstone; genetic mechanism; sealing mechanism of cap rocks; reservoir–cap combination; Panyu A Sag

Academic Editor: Jan Golonka

Received: 3 October 2025
Revised: 25 November 2025
Accepted: 4 December 2025
Published: 7 December 2025

Citation: Zhou, Y.; Peng, G.; Zhang, W.; Qiu, X.; Li, Z.; Wang, K.; Que, X.; Jia, P. Genetic and Sealing Mechanisms of Calcareous Sandstones in the Paleogene Zhuhai–Enping Formations, Panyu A Sag, Pearl River Mouth Basin. *Minerals* **2025**, *15*, 1285. https://doi.org/10.3390/min15121285

1. Introduction

Calcareous cement is one of the most widely distributed types of cement in clastic rock reservoirs. Its formation and distribution play a significant controlling role in reservoir physical properties, hydrocarbon migration and accumulation [1,2]. The genetic mechanisms, development patterns, and impact on reservoir heterogeneity of carbonate cementation have been central topics in reservoir geology and diagenetic dynamics research. Previous studies have often approached the precipitation and dissolution mechanisms of carbonates from

perspectives such as water–rock interactions, organic-inorganic interactions, and material exchange between sandstones and mudstones, utilizing thermodynamic and geochemical methods [3–5]. For instance, Barnes et al. [6] and Taylor and Macquaker [7] emphasized the influence of organic acids and thermochemical sulfate reduction (TSR) on carbonate solubility, while Lynch [8] and Rlykke [9] established temporal evolution models for cement development based on diagenetic sequences. Tan et al. [10] systematically summarized the geochemical characteristics and fluid sources of carbonate cements in different basin settings, pointing out that the sources of calcium ions include the decomposition of bioclasts, the dissolution and alteration of feldspar and other aluminosilicate minerals, as well as calcium ions originally present in depositional water and pore water [11–13]. Lee et al. (2021) pointed out the carbonates were close to the densest packing by mechanical compaction at a burial depth of 750 m, and major porosity deviations are associated with dolomitization, dolomitic cementation, aragonite needle-rich mud and non-skeletal grains [14].

In formations with high sand content (sand content > 80%), the lack of mudstone cap rocks and weak lateral sealing capacity of faults make the effective preservation of oil and gas a key challenge in exploration. Calcareous cemented layers often develop as dense, discontinuous interlayers within sand bodies. These layers not only control fluid flow pathways within the reservoir, leading to complex oil-water relationships and the distribution of residual oil [15,16], but may also act as a novel type of "internal cap", providing local cap rock functionality for hydrocarbon accumulation [17]. Previous studies on diagenesis in the sandstones of the Pearl River Mouth Basin indicate that the development of carbonate cements is a key factor leading to the densification of deep reservoirs in the Zhuhai Formation [18,19]. The distribution of calcareous cementation within sand bodies exhibits significant heterogeneity: sandstones adjacent to mudstones undergo preferential cementation due to intense water–rock reactions, forming dense layers, while conversely preserving the primary porosity of the underlying sand bodies [20]. The development of calcareous interbeds within sand bodies is mainly influenced by both sedimentary and diagenetic processes, with bioclasts serving as the primary source of calcium, supplemented by sources such as feldspar dissolution and silicate mineral hydration [1,16,17]. However, existing research predominantly regards calcareous cemented bodies as heterogeneous elements affecting reservoir quality, while systematic investigation into their sealing capacity as potential cap rocks, their formation mechanisms, spatial distribution, and dynamic effectiveness during accumulation processes remains lacking.

Panyu A Sag is located in the southern part of the Xijiang Sag, Zhu I Depression, and is a typical "small but rich" hydrocarbon-generating sag with high source rock potential. In recent years, significant breakthroughs have been made in drilling the Paleogene Zhuhai–Enping formations (with an overall sandstone content of 80%–95%) in Panyu A Sag, discovering proven in-place reserves exceeding 50 million tons [21]. Exploration practices have revealed that both mudstone and calcareous sandstone serve as two types of seals in the Zhuhai–Enping formations of the Panyu A Sag, with calcareous sandstone playing a critical role in sealing hydrocarbon accumulations. This study focuses on the widely developed dolomitic sandstone and anhydritic sandstone in the Zhuhai–Enping formations of the area. It aims to transcend the traditional perception that views calcareous cement merely as a factor influencing reservoir quality, and instead, delves into its sealing mechanisms and effectiveness in sand-rich settings. By integrating petrological, geochemical, and petroleum geological methods, this research seeks to unravel the genetic mechanisms, distribution patterns, and controlling effects of calcareous cemented layers on hydrocarbon accumulation. The findings are expected to address current research limits in "self-sealing sandstone layers" and provide new geological insights and predictive models for hydrocarbon exploration in sand-rich regions.

2. Regional Geological Background

2.1. Structural Location

The Pearl River Mouth Basin, as one of the most important petroliferous basins, is located on the northern continental margin of the South China Sea and is a Mesozoic-Cenozoic extensional basin [22]. Its formation and evolution are largely controlled by the rifting and spreading processes of the South China Sea. During the Paleocene to Eocene, this region underwent multiple phases of rifting, accompanied by lithospheric extension, fault development, and localized magmatic activity, resulting in the formation of several NE-trending dustpan-shaped sags and half-graben structures [23]. The Pearl River Mouth Basin exhibits a structural framework of "three uplifts and three depressions," which are divided from north to south into the Northern Fault Zone, Northern Depression Zone, Central Uplift Zone, Central Depression Zone, Southern Uplift Zone, and Southern Depression Zone [24]. The Zhu I Depression, located within the Northern Depression Zone of the Pearl River Mouth Basin, is the most significant oil-producing area in the basin. From west to east, it comprises the Enping Sag, Xijiang Sag, Huizhou Sag, Lufeng Sag, and Hanjiang Sag, which are separated by NW-trending low uplifts (Figure 1a).

The Panyu A Sag is located in the southern part of the Xijiang Sag. Its formation and evolution are controlled by the NE-SW trending boundary faults (Figure 1b). During the Paleogene, it experienced multiple tectonic movements, including the Shenhu tectonic movement, the first episode of the Zhuqiong tectonic movement, the Huizhou tectonic movement, and the second episode of the Zhuqiong tectonic movement [25,26] (Figure 1c). These events led to multiple intense phases of uplift and erosion within the sag, resulting in its current anti-"L" shaped distribution pattern, which is narrow in the NE direction and wide in the SW direction. The Panyu A Sag is bounded by the Dongsha Uplift to the east, adjacent to the Xien Low Uplift to the west, and bordered by the Panyu Low Uplift to the south. It can be further subdivided into the Northern Sub-sag, Southern Sub-sag, and Northwestern Sub-sag (Figure 1b).

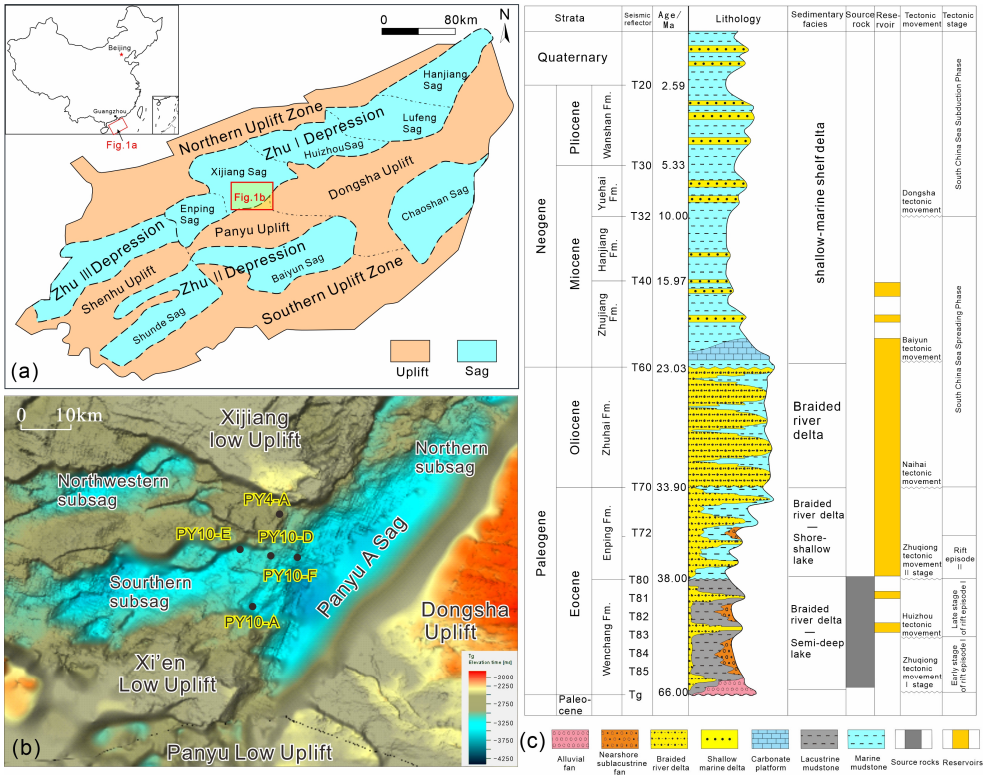

Figure 1. Structural unit subdivision of the Pearl River Mouth Basin (**a**); Basement topography and structural unit subdivision of the Panyu A Sag (**b**); Stratigraphic column of the Panyu A Sag (**c**) (Modified from [27]).

2.2. Stratigraphy

The basin basement consists of Early Cretaceous granite. Overlying the basement, the Cenozoic sedimentary strata from oldest to youngest are as follows: the Eocene Wenchang Formation (E_2w) and Enping Formation (E_2e), the Oligocene Zhuhai Formation (E_3z), the Miocene Zhujiang Formation (N_1z), Hanjiang Formation (N_1h), and Yuehai Formation (N_1y), the Pliocene Wanshan Formation (N_2w), and the Quaternary (Q) [21]. Among these, the Wenchang Formation and lower Enping Formation deposited during the rift phase represent continental facies, while the upper Enping Formation and Zhuhai Formation formed during the rift-sag transition phase exhibit marine–terrestrial transitional facies. Strata above the Zhujiang Formation deposited during the sag phase are characterized by marine facies [28]. Within the depression, hydrocarbon source rocks are primarily developed in the Wenchang Formation, while high-quality reservoirs occur in the Enping, Zhuhai, Zhujiang, and Hanjiang Formations. Overall, the petroleum system presents a "source rocks below with reservoirs above" accumulation model [27] (Figure 1c).

2.3. Sedimentary Characteristics

The Enping Formation in the Panyu A Sag is characterized by deltaic sandstone deposits, with locally developed shallow lacustrine depositional systems [29]. In the lower member of the Enping Formation, it inherited the active fault characteristics of the Wenchang Formation, with the depositional center largely consistent with that of the Wenchang period. In the upper member of the Enping Formation, fault activity significantly weakened, marking a transition period from faulting to depression. NW-trending faults along the western margin began to control sedimentation, leading to a gradual migration of the depositional center toward the southwestern side. The thickness of the strata in the depositional center is 3 to 5 times greater than that in the marginal areas [30]. The Zhuhai Formation represents a transitional deposit from terrestrial to marine environments, comprising a sequence of deltaic and coastal deposits, with relatively well-developed sandstones (Figure 1c).

Drilling data reveal that the lower member of the Enping Formation in the Panyu 4 Sag ranges from 131 to 280 m in thickness, with sand content of 89.6%–98.4%. The lithology is dominated by thick-bedded, pebbly medium- to coarse-grained sandstones, with intercalations of calcareous siltstones and thin mudstone layers. The upper member of the Enping Formation exhibits a thickness of 211–213 m and sand content of 78.1%–86.8%, primarily composed of medium- to fine-grained sandstones, calcareous sandstones, and mudstones. The Zhuhai Formation ranges from 429 to 639 m in thickness, with sand content of 65%–78%. Sandstone units consist mainly of thick-bedded, pebbly coarse sandstones, coarse sandstones, medium sandstones, and fine sandstones, interbedded with thin layers of calcareous medium- to fine-grained sandstones.

3. Materials and Methods

A total of 182 core samples from wells PY10-A, PY10-D, and PY10-F were collected for this study, encompassing typical intervals from the third member of the Zhuhai Formation, as well as the upper and lower members of the Enping Formation, with a focus on calcareous sandstones. Petrological and mineralogical analyses were first conducted using polarized light microscopy and scanning electron microscopy (TM4000plus, Hitachi, Tokyo, Japan). A total of 31 samples from Well PY10-A and 18 samples from Well PY10-F were selected for analysis of major and trace elements. Major element analysis was performed using a PANalytical Axios mAX wavelength-dispersive X-ray fluorescence (Bruker Corporation, Berlin, Germany) spectrometer, while trace element analysis was carried out with a NexION 300D inductively coupled plasma mass spectrometer (PerkinElmer, Waltham, MA, USA).

Quality control measures included duplicate analyses of selected samples and certified reference materials. The relative standard deviation (RSD) for all elemental measurements was maintained below 10%, with both instrumental results and standard deviations falling within acceptable limits.

Next, 17 sandstone samples with well-developed carbonate cements were selected for further carbon and oxygen isotope analysis. Six samples from well PY10-A underwent in situ carbon–oxygen isotope analysis using laser ablation-stable isotope analyzer (Picarro Inc., Santa Clara, CA, USA). This system consists of a CETAC laser ablation unit coupled with a microscopic imaging system and a Delta isotope mass spectrometer. Additionally, 11 samples from wells PY10-A, PY10-D, and PY10-F were analyzed for bulk rock carbon and oxygen isotope ratios. The measured isotope ratios are reported as $\delta^{13}C$ and $\delta^{18}O$ values relative to the PDB standard in per mil (‰), with an analytical precision of 0.02‰. Detailed sample information and analytical results are presented in Tables 1 and 2. The in situ isotope analyses were conducted at the Zhanjiang Laboratory of CNOOC's Experimental Center, while bulk rock isotope analyses were performed at the National Key Laboratory of Petroleum Resources and Engineering at China University of Petroleum (Beijing).

Table 1. Major element analysis of Zhuhai–Enping Formation in Well PY10-A.

Strata	Depth (m)	Al_2O_3 /%	CaO /%	Fe_2O_3 /%	K_2O /%	MgO /%	MnO /%	Na_2O /%	P_2O_5 /%	TiO_2 /%	SiO_2 /%
E_3z_1	3005	11.9	0.93	4.60	2.66	1.29	0.14	0.43	0.04	0.62	72.7
	3055	11.9	0.28	5.11	2.64	1.20	0.17	0.39	0.03	0.75	71.8
	3115	9.70	0.54	3.02	2.58	1.09	0.02	0.43	0.01	0.52	78.4
	3150	14.8	0.20	4.73	3.11	1.55	0.03	0.58	0.03	0.77	68.3
	3195	9.85	0.50	3.43	2.52	1.19	0.04	0.56	0.02	0.55	77.4
E_3z_2	3270	12.9	0.50	4.49	3.17	1.67	0.04	0.62	0.13	0.70	71.7
	3310	7.84	0.62	3.28	2.66	1.08	0.06	0.60	0.04	0.37	80.2
	3375	8.51	0.44	2.20	3.02	1.02	0.03	0.76	0.05	0.34	80.3
	3405	10.7	1.39	3.02	3.33	1.41	0.04	0.67	0.04	0.42	74.4
E_3z_3	3440	10.6	0.69	3.77	3.10	1.74	0.05	0.60	0.06	0.45	75.0
	3470	6.34	2.07	2.00	2.83	1.50	0.08	0.67	0.04	0.16	80.5
	3505	5.84	5.49	3.46	2.72	3.41	0.26	0.65	0.04	0.14	68.7
	3525	7.08	5.47	4.89	2.61	3.59	0.24	0.65	0.09	0.26	67.3
	3535	7.34	0.47	2.47	2.90	1.03	0.02	0.77	0.03	0.29	81.3
	3560	11.9	0.76	4.24	3.06	1.92	0.05	0.62	0.04	0.61	72.3
	3565	8.64	0.38	3.30	3.07	1.21	0.02	0.73	0.05	0.33	78.7
	3580	5.86	0.32	1.50	2.60	0.62	0.01	0.66	0.02	0.15	86.0
	3640	6.30	2.45	1.79	3.18	0.71	0.01	0.74	0.01	0.08	82.7
	3645	17.9	0.18	4.26	3.83	1.80	0.02	0.53	0.01	0.74	65.4
E_2e_1	3685	6.53	6.49	5.13	2.79	4.06	0.38	0.64	0.02	0.18	64.1
	3690	5.71	6.14	5.76	2.49	3.93	0.36	0.57	0.08	0.15	69.3
	3700	5.70	8.34	4.71	2.41	4.53	0.44	0.64	0.06	0.18	64.4
	3705	6.05	8.58	6.70	2.49	4.37	0.59	0.65	0.27	0.20	62.0
	3715	7.24	0.52	3.73	2.57	1.22	0.04	0.65	0.02	0.37	81.1
	3720	9.75	0.63	5.23	3.11	1.57	0.06	0.70	0.07	0.41	76.2
	3730	5.50	6.31	5.13	2.40	3.49	0.51	0.68	0.03	0.17	72.4
	3750	6.62	1.32	2.25	2.74	1.24	0.08	0.83	0.03	0.32	79.8
	3760	10.6	0.40	3.43	3.17	1.38	0.03	0.82	0.05	0.49	76.2
	3785	9.22	0.24	1.75	3.58	0.66	0.01	0.83	0.04	0.32	79.8
E_2e_2	3925	6.08	3.28	1.88	3.07	1.87	0.12	0.69	0.01	0.12	77.6
	3945	5.07	3.54	1.66	2.38	1.68	0.12	0.51	0.00	0.11	79.9

Table 2. Trace element analysis of Zhuhai–Enping Formation in Well PY10-A.

Strata	Depth (m)	V/ ppm	Ni/ ppm	Cu/ ppm	Ga/ ppm	Rb/ ppm	Sr/ ppm	Y/ ppm	Zr/ ppm	Ba/ ppm	B/ ppm	Sr/Cu	Sr/Ba	B/Ga	V/(V + Ni)	Zr/Y	Rb/Zr
E_3z_1	3005	56.0	18.8	22.0	12.9	122.6	91	28.6	257	8052	52.5	4.145	0.011	4.061	0.749	8.994	0.476
	3055	56.9	16.9	20.1	13.4	125	80	31.3	261	8117	49.9	3.970	0.010	3.723	0.771	8.331	0.477
	3115	45.0	14.4	16.0	10.6	120	86	26.4	239	11,416	39.7	5.372	0.008	3.748	0.757	9.046	0.501
	3150	61.8	20.8	24.1	15.94	149.3	78	33.8	266	5708	65.2	3.243	0.014	4.089	0.748	7.853	0.562
	3195	46.6	14.9	15.9	10.58	115.0	68	24.0	245	6171	54.6	4.291	0.011	5.158	0.758	10.205	0.470
E_3z_2	3270	55.6	19.4	17.4	13.16	139.8	76	30.7	247	5283	65.1	4.374	0.014	4.946	0.741	8.020	0.567
	3310	36.1	15.4	15.3	8.10	114.5	77.9	21.5	216	10,101	37	5.103	0.008	4.504	0.701	10.068	0.530
	3375	35.3	13.9	13.0	8.36	120.8	84	21.2	210	11,342	39.6	6.510	0.007	4.738	0.717	9.921	0.575
	3405	43.4	17.7	14.8	10.72	141.7	116	21.0	228	9860	36.2	7.843	0.012	3.373	0.710	10.847	0.621
E_3z_3	3440	46.6	17.0	13.8	11.0	139	77	23.8	227	7870	53.6	5.567	0.010	4.877	0.733	9.538	0.612
	3470	26.9	11.2	10.3	6.1	115	94	16.4	187	8217	15.8	9.077	0.011	2.583	0.706	11.420	0.615
	3505	30.1	12.6	13.7	5.6	105	68	19.2	179	6709	16.3	4.994	0.010	2.932	0.705	9.340	0.586
	3525	42.7	20.3	11.9	7.2	106	70	24.2	211	6725	21.9	5.899	0.010	3.028	0.678	8.731	0.501
	3535	30.8	12.2	11.8	7.4	120	74	19.2	199	9603	28.8	6.283	0.008	3.896	0.717	10.415	0.603
	3560	49.9	17.2	17.7	12.0	132	69	28.6	259	4797	70.5	3.877	0.014	5.894	0.744	9.048	0.509
	3565	36.1	13.9	12.6	8.50	122.7	75	23.7	217	9414	25.8	5.925	0.008	3.033	0.723	9.132	0.566
	3580	24.7	9.0	9.1	5.7	111	66	14.7	189	6808	25.2	7.243	0.010	4.422	0.734	12.848	0.586
	3640	21.4	6.6	31.1	5.34	114.3	157.7	12.4	172	6354	9.3	5.066	0.025	1.741	0.763	13.823	0.666
	3645	65.4	20.1	23.7	18.3	171	76	35.9	260	4496	60.3	3.208	0.017	3.300	0.765	7.252	0.655
E_2e_1	3685	35.9	13.2	9.9	6.4	104	75.5	19.8	199	6309	14.3	7.646	0.012	2.218	0.731	10.027	0.524
	3690	44.5	14.5	8.6	5.8	91	73.4	21.5	184	6761	12.0	8.559	0.011	2.063	0.755	8.555	0.493
	3700-	30.8	11.0	9.3	5.4	89	82.1	21.1	199	7759	12.8	8.798	0.011	2.389	0.737	9.416	0.445
	3705	38.1	14.3	14.9	6.0	89	77.1	24.7	195	6123	14.4	5.193	0.013	2.415	0.727	7.888	0.456
	3715	32.3	10.6	15.2	7.2	95	63.4	25.5	260	6699	38.1	4.175	0.009	5.324	0.753	10.199	0.365
	3720	46.2	17.6	14.1	9.6	120	68.3	27.7	257	5868	45.2	4.850	0.012	4.719	0.724	9.288	0.465
	3730	37.3	12.4	8.9	5.5	89	65.9	17.7	208	5586	18.0	7.374	0.012	3.248	0.750	11.720	0.429
	3750	34.1	11.5	13.6	6.7	96	119.3	21.7	289	25,202	27.1	8.752	0.005	4.039	0.748	13.350	0.332
	3760	42.1	14.9	14.5	10.3	115	83.6	27.0	288	11,374	56.1	5.764	0.007	5.441	0.739	10.681	0.400
	3785	30.5	9.5	11.4	8.5	117	98.3	20.7	243	9907	27.8	8.595	0.010	3.273	0.762	11.761	0.482
E_2e_2	3925	22.7	5.9	9.3	5.4	93	127.0	12.0	176	16,288	9.4	13.589	0.008	1.745	0.794	14.685	0.531
	3945	23.7	27.2	37.6	4.6	78.7	126	11.6	173	16,400	13.4	3.365	0.008	2.920	0.465	14.897	0.455

Three calciferous sandstone samples and 11 reservoir samples were selected for porosity and permeability tests and high-pressure mercury injection analysis. The porosity and permeability were measured from 2.5 cm diameter core plugs from the reservoir intervals using a nitrogen permeameter (Core Laboratories, Houston, TX, USA). The dry and clean core samples were placed in the permeameter and injected with nitrogen at confining pressures of 100 and 400 psi. The high-pressure mercury injection experiment was performed on a PoreMaster PM33-13 mercury porosimeter (Micromeritics, Norcross, GA, USA). Three calcareous sandstone samples and two mudstone samples were selected for breakthrough pressure measurements using the pulse decay method. This technique involves applying a high gas injection pressure at the inlet end that exceeds the rock's critical breakthrough pressure, enabling rapid gas penetration into the core. During gas injection, the outlet end maintains a constant-volume pressure monitoring chamber. The pressure differential across the core is continuously recorded as gas enters the system. This process displaces pore water into the monitoring chamber, resulting in progressive pressure buildup at the outlet. When the outlet pressure stabilizes, the pressure difference between the two ends represents the critical gas breakthrough pressure measured by the pulse decay method. The porosity and permeability tests, high-pressure mercury injection experiment and pulse decay breakthrough pressure tests were conducted at the National Key Laboratory of Petroleum Resources and Engineering, China University of Petroleum (Beijing).

4. Results

4.1. Petrological Characteristics of Calcareous Sandstones

The calcareous sandstone in the Enping–Zhuhai formations of the study area has a single-layer thickness of 1–3 m. The lithology is predominantly dolomitic medium- to fine-grained feldspathic quartz sandstone and feldspathic lithic sandstone (Figure 2). The quartz content ranges from 44.5% to 80% (avg. 67.6%), feldspar content ranges from 4%

to 32% (avg. 15.5%), and lithic fragment content ranges from 4% to 35.5% (avg. 16.9%). The lithic fragments are predominantly volcanic in origin, with content ranging from 2.5% to 33.5% (avg. 13.2%). Grain contacts are mainly point-to-line, and roundness is primarily subangular to subrounded. Overall, pore development is poor, with measured porosity ranging from 4.4% to 9.5% and permeability ranging from 0.02 mD to 0.19 mD. In the southern area, the calcareous sandstone in well PY10-A is mainly cemented by (ferroan) dolomite (content 7.5%–43%), exhibiting various occurrences such as micritic, microcrystalline, fine-crystalline, and coarse-crystalline types. In the northern area, wells PY10-D and PY10-F are primarily cemented by anhydrite (content 6%–32%), which often fills large pores and forms polkilotopic cementation between grains.

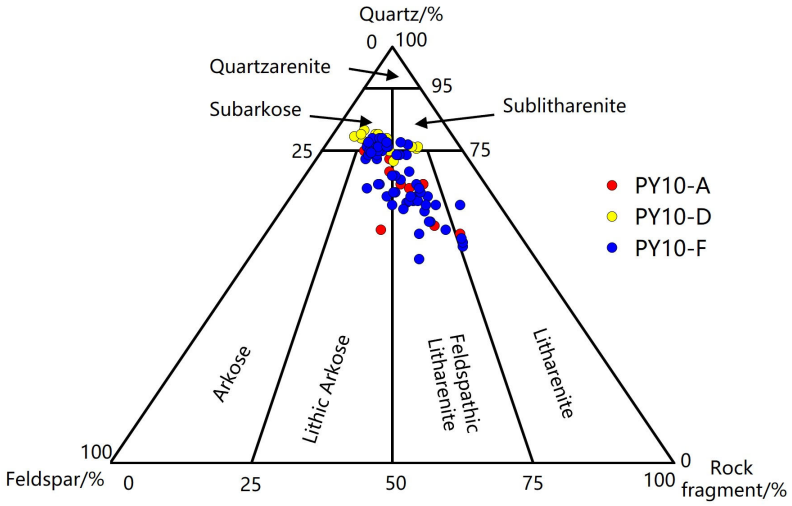

Figure 2. Petrographic composition ternary diagram of calcareous sandstones in the Panyu A Sag.

Glauconite is abundant in the study area (Figure 3a–c), with a content ranging from 1.5% to 12%. It occurs as green elliptical grains with well-preserved morphology and shows no evidence of plastic deformation (Figure 3c). Microscopic examination reveals diverse bioclasts including echinoderms (Figure 3d–e), foraminifera (Figure 3f–g), and bivalves (Figure 3h–i), with minor preservation of intraparticle pores within bioclasts.

4.2. Calcareous Cement Types and Characteristics

4.2.1. Dolomite

Dolomite remains unstained when treated with a mixed solution of potassium ferricyanide and alizarin red S. It predominantly exhibits basal cementation, with subordinate porous cementation and grain replacement textures. Petrographically, dolomite cements are classified into micritic dolomite, euhedral-subhedral silt-to-fine crystalline dolomite, and anhedral coarse crystalline dolomite.

(1) Micritic Dolomite

Micritic dolomite predominantly developed in the upper section of the Enping Formation in Well PY10-A, with contents ranging from 29% to 32%. It mainly exhibits basal cementation. The micritic dolomite usually forms isopachous micritic envelopes around grains, primarily coating bioclasts and intraclasts (Figure 4a–c). Intense micritization obliterates original internal structures of some bioclasts, forming micritic peloids. This micritic dolomite typically precipitates prior to syntaxial overgrowths on cements and bioclasts, serving as a diagnostic indicator of syngenetic marine seafloor diagenesis. The micritization of carbonate grains represents a key diagenetic feature in stagnant marine phreatic zones and also evidence of relatively slow sediment aggradation rates. Under these con-

ditions, intergranular carbonate cementation is underdeveloped, allowing ample time for algal/fungal perforation [31,32].

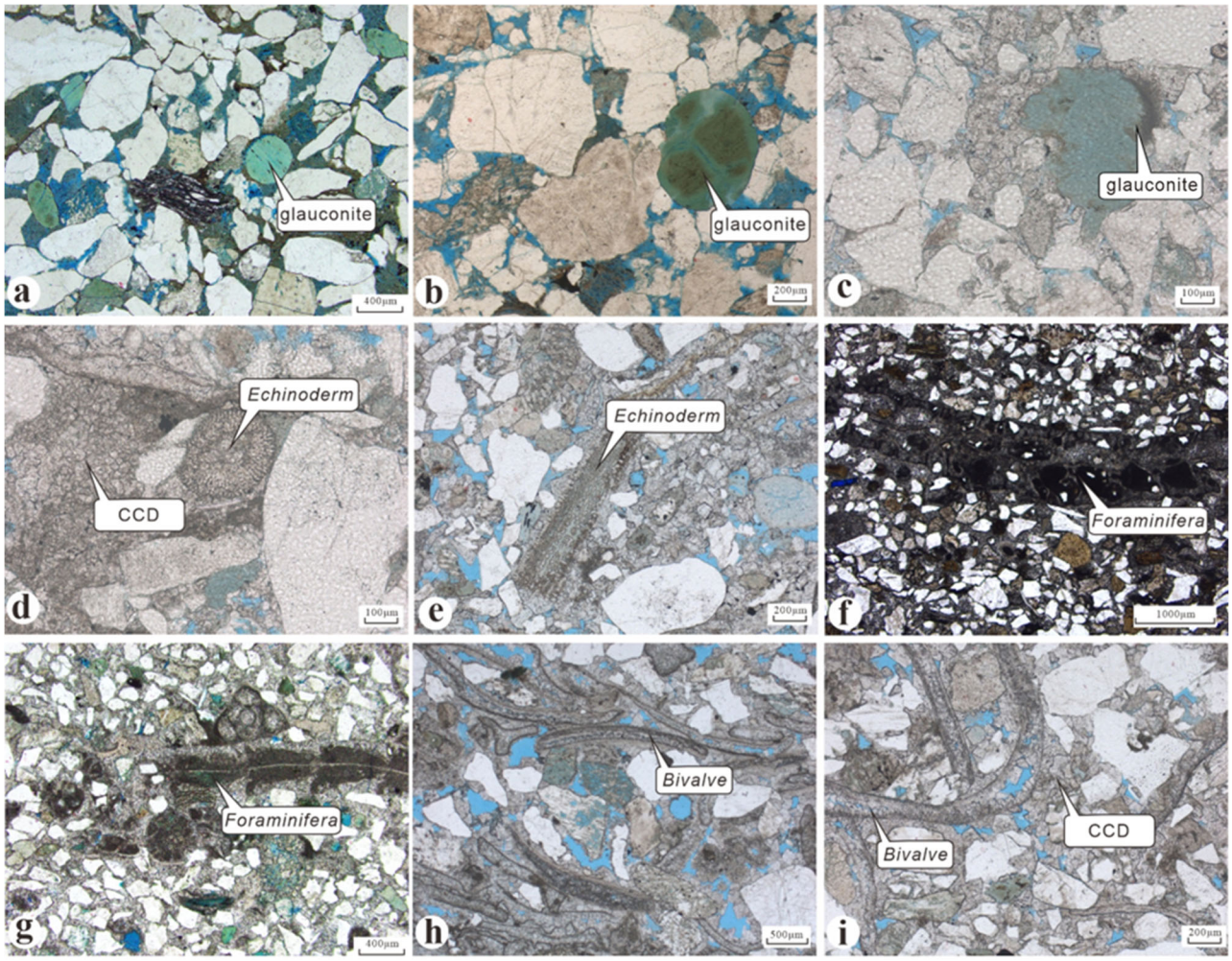

Figure 3. Microstructural Characteristics of Glauconite and Bioclasts in the Zhuhai and Enping Formations, Panyu A Sag. (**a**) Scattered elliptical green glauconite grains, E_3z (Zhuhai Fm. Mb. 2), Well PY10-D, 3130 m, blue epoxy, PPL; (**b**) Minor elliptical glauconite particles, E_3z, Well PY10-D, 3225 m, blue epoxy, PPL; (**c**) Sparse glauconite grains (partially altered), E_2e, Well PY10-F, 3698.95 m, blue epoxy, PPL; (**d**) Pervasive micritic to fine-crystalline dolomite filling intergranular pores and cementing grains, with minor echinoderm debris, E_2e, Well PY10-F, 3697.2 m, blue epoxy, PPL; (**e**) Isolated echinoderm bioclasts, E_2e, Well PY10-F, 3700.95 m, blue epoxy, PPL; (**f**) Micritic dolomite cementing grains with foraminiferal bioclasts, E_2e, Well PY10-A, 3686 m, blue epoxy, PPL; (**g**) Minor foraminifera fragments, E_2e, Well PY10-A, 3703.5 m, blue epoxy, PPL; (**h**) Abundant bivalve bioclasts retaining body cavities, E_2e, Well PY10-F, 3702.2 m, blue epoxy, PPL; (**i**) Dominant bivalve debris with preserved internal molds, E_2e, Well PY10-F, 3703.2 m, blue epoxy, PPL. PPL: plane-polarized light. Abbreviations: CCD: coarse crystalline dolomite.

(2) Silt to Fine-crystalline Dolomite

Silt to fine-crystalline dolomite is the most widespread dolomite texture in the study area, it occurs as crystalline clusters with interconnected or partially overlapping crystals (Figure 4f). It usually evolves from intergranular micritic dolomite precursors. Progressive burial depth and continuous dolomitizing fluid supply drive crystal overgrowth and structural reorganization of micritic matrix, ultimately developing cohesive clusters of planar-faced euhedral-subhedral dolomite crystals. Petrographic observations reveal dolomite replacement textures affecting quartz and glauconite grains (Figure 4d,e). Both

micritic dolomite and euhedral-subhedral silt-sized to fine-crystalline dolomite represent products of shallow-burial dolomitization.

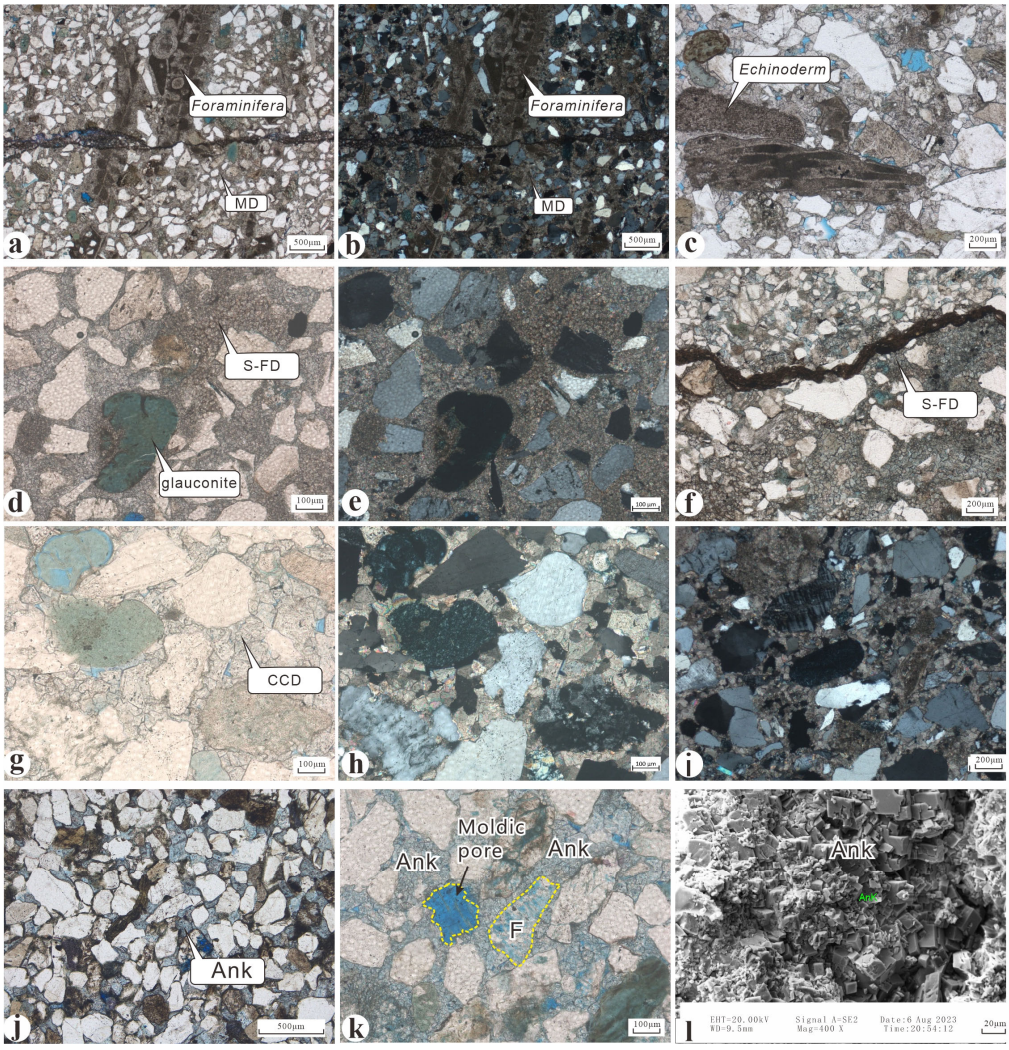

Figure 4. Microstructural characteristics of dolomite/ankerite cementation in the Zhuhai and Enping Formations, Panyu A Sag. (**a**) Micritic dolomite replacing foraminiferal bioclasts in aggregated form, E2e (Upper Enping Fm.), Well PY10-A, 3703.5 m, blue epoxy-impregnated, PPL; (**b**) Same view as (**a**) under XPL; (**c**) Pervasive micritic dolomite filling intergranular pores and cementing grains, with minor bioclasts (foraminifera, echinoderms, brachiopods, bivalves), E2e, Well PY10-F, 3702.95 m, blue epoxy, PPL; (**d**) Basal-fill dolomite cementation with micritic texture, E2e, Well PY10-A, 3695.5 m, blue epoxy, PPL; (**e**) Same view as (**d**) under XPL; (**f**) Dominant subhedral silt-to fine-crystalline dolomite cementing grains, E2e, Well PY10-A, 3767 m, blue epoxy, PPL; (**g**) Dolomite infilling interparticle spaces and cementing grains, showing minor elliptical green glauconite (compressed/deformed, partially altered to clay minerals), E2e, Well PY10-F, 3697.95 m, blue epoxy, PPL; (**h**) Same view as (**g**) under XPL; (**i**) Coarse-crystalline dolomite extensively occupying intergranular pores, with minor glauconite alteration and echinoderm debris, E2e, Well PY10-F, 3696.95 m, blue epoxy, XPL; (**j**) Ankerite cementing grains through pervasive pore-filling, E2e, Well PY10-D, 3604 m, blue epoxy, PPL; (**k**) Medium-to coarse-crystalline ankerite cementing grains exhibiting feldspar dissolution, E2e, Well PY10-A, 3686 m, blue epoxy, PPL; (**l**) Aggregated rhombohedral ankerite (Ank) clusters, E3z, Well PY10-A, 3356 m, SEM. PPL: plane-polarized light; XPL: cross-polarized light; SEM: scanning electron microscope. Abbreviations: MD: micritic dolomite, S-FD: silt-to-fine crystalline dolomite, CCD: coarse crystalline dolomite, Ank: ankerite, F: feldspar.

(3) Anhedral Coarse-crystalline Dolomite Anhedral coarse-crystalline dolomite exhibits variable crystal sizes ranging from fine to coarse, with curved anhedral boundaries.

Under plane-polarized light, crystal surfaces appear turbid with indistinct zoning, while crossed polars reveal uniform extinction (Figure 4g–i). The coarse-crystalline dolomite can be formed through the recrystallization of pre-existing silt-sized to fine-crystalline dolomite, or through the recrystallization or replacement reactions of micritic dolomite when encountering high-temperature dolomitizing fluids during deep burial stages. Enhanced supersaturation of dolomite in fluids (specifically elevated Mg^{2+}/Ca^{2+} ratios) drives development of mosaic textures with characteristic curvilinear crystal contacts [33].

4.2.2. Ankerite

Ankerite is defined as a dolomite-group mineral where over 50% of magnesium ions are substituted by iron ions [34,35]. It stains blue when treated with a mixed solution of potassium ferricyanide and alizarin red S. Ankerite develops primarily as porous cementation binding detrital grains (Figure 4j,k), and the rhombohedral ankerite crystals exhibit polikilotopic distribution (Figure 4i) under scanning electron microscopy (SEM). Additionally, authigenic quartz is replaced by ankerite (Figure 4k), suggesting alterations in diagenetic fluid chemistry.

4.2.3. Anhydrite

In the southern area of Panyu A Sag, anhydrite occurred in Wells PY10-A is predominantly developed in the upper member of the Enping Formation and the 3rd Member of the Zhuhai Formation. Conversely, in the northern area of Panyu A Sag, anhydrite occurred in Wells PY10-D and PY10-F ubiquitously across all stratigraphic members.

Anhydrite commonly fills large intergranular pores and occurs as patchy or basal cementation binding detrital grains (Figure 5), with contents ranging from 9% to 26%. Its strongly heterogeneous cementation patterns (Figure 5a,b) compromise its effectiveness as a regional seal. Detrital grains cemented by anhydrite predominantly exhibit point-to-line contacts and point contacts (Figure 5c,d), indicating limited compaction. This reflects anhydrite precipitation during shallow-burial stages (syngenetic to eogenetic periods) within evaporative depositional settings. Petrographic observations reveal anhydrite commonly associated with quartz dissolution (Figure 5e) or replacement of quartz grains (Figure 5f), indicating precipitation in an early-stage alkaline diagenetic environment. According to previous studies, the δ^{34}SV-CDT values of Paleogene anhydrite in the Zhu I Depression range from 18.12‰ to 31.71‰, exhibiting broad variability within the isotopic range of marine evaporite sulfates. This indicates formation in evaporative brines during initial burial [36].

4.3. Geochemical Characteristics

4.3.1. Major Elements

The major elemental contents of the 31 core samples from Well PY10-A are shown in Table 1. The MgO content is 0.4%~4.53% (avg. 1.86%), the CaO content is 0.18%~8.58% (avg. 2.14%), the Al_2O_3 content is 5.5%~17.9% (avg. 8.87%), the SiO_2 content is 61.94%~85.99% (avg. 74.68%), the K_2O content is 2.40%~4.97% (avg. 2.95%), the MnO content is 0.008%~0.59% (avg. 0.13%), the Na_2O content is 0.39%~1.27% (avg. 0.67%), the TiO_2 content is 0.08%~0.77% (avg. 0.36%), and the P_2O_5 content is 0.007%~0.27% (avg. 0.047%).

4.3.2. Trace Elements

The trace element contents of the 31 core samples from Well PY10-A and 18 core samples from Well PY10-D are shown in Tables 2 and 3. For samples from Well PY10-A, the Sr/Cu ratio ranges from 0.39 to 30.0 (avg. 11.9), the Sr/Ba ratio ranges from 0.012 to 0.177 (avg. 0.065), the B/Ga ratio ranges from 1.74 to 5.89 (avg. 3.64), the V/(V + Ni) ratio ranges from 0.46 to 0.79 (avg. 0.73), the Zr/Y ratio ranges from 7.25 to 15.14 (avg. 20.39), the

Rb/Zr ratio ranges from 0.33 to 0.82 (avg. 0.53) (Table 2). For samples from Well PY10-D, the Sr/Cu ratio ranges from 2.3 to 5.77 (avg. 3.32), the Sr/Ba ratio ranges from 0.003 to 0.013 (avg. 0.006), the B/Ga ratio ranges from 1.48 to 6.92 (avg. 4.13), the V/(V + Ni) ratio ranges from 0.72 to 0.83(avg. 0.77), the Zr/Y ratio ranges from 8.1 to 20.0 (avg. 12.53), the Rb/Zr ratio ranges from 0.44 to 0.75 (avg. 0.61) (Table 3).

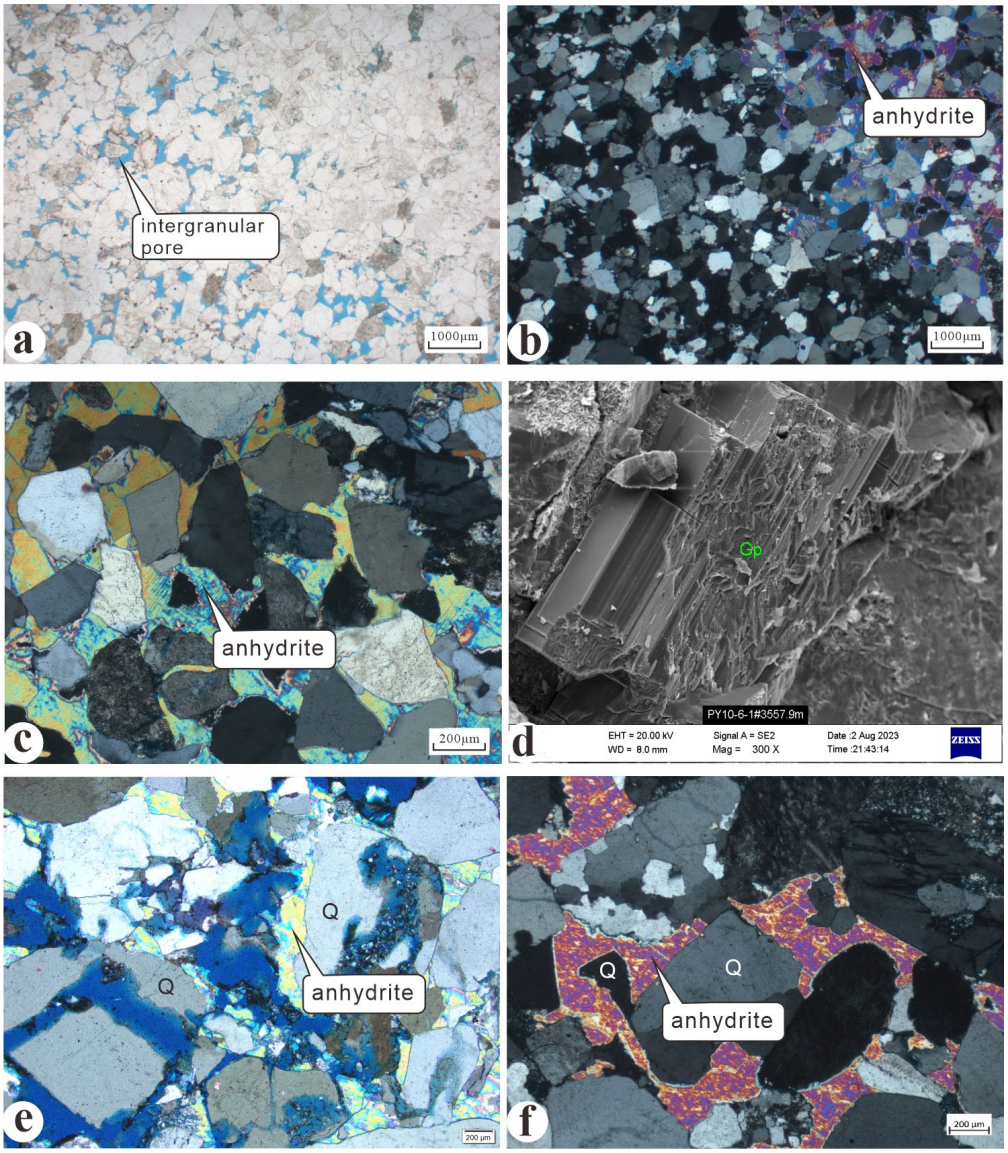

Figure 5. Microstructural characteristics of gypsum/anhydrite cementation in the Zhuhai and Enping Formations, Panyu A Sag. (**a**) Locally developed poikilotopic anhydrite cementing grains with patchy pore-filling, E2e, Well PY10-F, 3711.92 m, blue epoxy, PPL; (**b**) Same view as (**a**) under XPL; (**c**) Pervasive poikilotopic anhydrite occupying intergranular spaces and cementing grains, E3z, Well PY10-F, 3487 m, blue epoxy, XPL; (**d**) Tabular gypsum (Gp) crystals cementing grains, E3z, Well PY10-A, 3557.9 m, SEM; (**e**) Local anhydrite pore-filling with pronounced quartz dissolution, E2e, Well PY10-D, 3775.3 m, blue epoxy, XPL; (**f**) Extensive quartz grain dissolution with anhydrite cementation and pore-occlusion, E2e, Well PY10-D, 3735.8 m, blue epoxy, XPL. Abbreviations: PPL: plane-polarized light; XPL: cross-polarized light; SEM: scanning electron microscope; Gp: Gypsum, Q: Quartz.

Table 3. Trace element analysis of Zhuhai–Enping Formation in Well PY10-D.

Strata	Depth (m)	V/ ppm	Ni/ ppm	Cu/ ppm	Ga/ ppm	Rb/ ppm	Sr/ ppm	Y/ ppm	Zr/ ppm	Ba/ ppm	B/ ppm	Sr/Cu	Sr/Ba	B/Ga	V/(V + Ni)	Zr/Y	Rb/Zr
E_3z_1	2986	29.8	9.9	56.3	4.3	71	147	9.2	162	44,603	26.4	2.609	0.003	6.098	0.750	17.536	0.442
	3097	32.6	8.9	58.9	3.9	76	175	11.3	151	59,735	17.3	2.970	0.003	4.460	0.786	13.284	0.506
E_3z_2	3193	38.5	12.4	61.3	6.48	103.5	164	13.8	189	52,937	36.8	2.673	0.003	5.675	0.756	13.706	0.548
	3199	29.3	7.7	55.2	3.38	69.5	155	7.8	157	52,158	23.4	2.819	0.003	6.919	0.791	20.029	0.443
	3322	38.3	11.5	49.9	7.60	130.5	127	16.8	194	33,087	48.7	2.550	0.004	6.412	0.769	11.541	0.671
E_3z_3	3457	37.1	11.6	59.1	6.43	113.5	186.6	13.6	175	47,535	41	3.157	0.004	6.333	0.762	12.865	0.646
	3472	32.2	9.5	53.6	5.67	110.8	152	12.5	170	47,758	22.5	2.839	0.003	3.961	0.772	13.618	0.652
E_2e_1	3547	30.1	9.7	48.8	6.50	133.2	282	14.0	193	22,647	23.2	5.773	0.012	3.567	0.756	13.784	0.691
	3598	41.4	13.2	60.7	6.6	112	174	18.2	169	23,718	15.5	2.873	0.007	2.358	0.758	9.279	0.666
	3601	38.8	13.4	50.5	5.2	90	146	16.1	156	31,291	19.3	2.886	0.005	3.716	0.743	9.651	0.579
	3640	38.5	12.3	43.5	5.2	93	162	15.0	163	37,715	17.7	3.722	0.004	3.422	0.758	10.899	0.571
	3649	31.3	10.4	44.7	4.7	94	219	15.5	153	35,644	13.0	4.896	0.006	2.796	0.751	9.846	0.616
	3652	32.6	9.8	35.1	5.8	116	133	13.9	170	10,376	19.4	3.791	0.013	3.356	0.769	12.235	0.681
	3658	38.1	12.1	45.5	6.3	109	144	20.7	225	33,070	29.4	3.168	0.004	4.653	0.759	10.893	0.486
	3694	39.7	15.3	45.9	8.78	144.9	106	23.8	193	9324	26.2	2.302	0.011	2.983	0.722	8.101	0.752
	3700	31.2	8.7	37.3	6.5	114	96	15.6	184	15,786	27.1	2.562	0.006	4.191	0.781	11.802	0.619
E_2e_2	3988	54.8	11.3	48.9	14.78	169.7	142.8	26.0	239	23,063	21.9	2.921	0.006	1.482	0.829	9.164	0.711
	4024	24.0	6.0	51.0	5.9	102	263	8.9	154	22,233	11.2	5.158	0.012	1.893	0.801	17.308	0.662

4.3.3. Carbon and Oxygen Isotope Data

Through analysis of 19 in situ carbon–oxygen isotopes and 11 whole-rock carbon–oxygen isotopes, the in situ $\delta^{13}C_{PDB}$ values of Enping–Zhuhai formations in the study area range from −11‰ to −22‰ (avg. −14.95‰), while $\delta^{18}O_{PDB}$ values range from −2.2‰ to −10‰ (avg. −5.49‰) (Table 4). Whole-rock $\delta^{13}C_{PDB}$ values range from −10‰ to −11‰ (avg. −10.34‰), and $\delta^{18}O_{PDB}$ values range from −8‰ to −13‰ (avg. −10.47‰) (Table 5). There are obvious differences in carbon and oxygen isotopes of different lithologies. The $\delta^{13}C_{PDB}$ values of micritic dolomite range from −11.73‰ to −22.01‰ (avg. −16.84‰), and $\delta^{18}O_{PDB}$ values range from −2.25‰ to −4.24‰ (avg. −3.20‰). The $\delta^{13}C_{PDB}$ values of silt-to-fine crystalline dolomite range from −10.97‰ to −15.37‰ (avg. −13.59‰), and $\delta^{18}O_{PDB}$ values range from −5.62‰ to −7.28‰ (avg. −6.72‰). The $\delta^{13}C_{PDB}$ values of coarse crystalline dolomite range from −11.93‰ to −13.25‰ (avg. −12.44‰), and $\delta^{18}O_{PDB}$ values range from −9.15‰ to −10.02‰ (avg. −9.56‰).

Table 4. In situ Carbon and Oxygen Isotope Test Data of Calcareous Sandstone in the Zhuhai and Enping Formations from Well PY10-A, Panyu A Sag.

Strata	Depth (m)	Measured Point	Cement Types	$\delta^{13}C_{PDB}$ (‰)	$\delta^{18}O_{PDB}$ (‰)	$\delta^{18}O_{SMOW}$ (‰)	Z	Paleo-Temperature (°C)
E_3z	3518	1	CCD	−11.94	−9.16	21.44	98.32	87.90
		2	S-FD	−14.38	−7.28	23.36	94.22	72.64
		3	CCD	−12.12	−9.52	21.06	97.72	91.14
	3565.3	1	CCD	−17.62	−2.64	28.14	89.94	41.98
		2	S-FD	−14.56	−6.92	23.74	94.06	69.88
		3	S-FD	−10.98	−6.78	23.88	101.48	68.84
		4	MD	−22.01	−3.20	27.58	80.64	45.20
E_2e	3695.5	1	S-FD	−12.82	−6.50	24.16	97.84	66.86
		2	S-FD	−11.76	−7.24	23.40	99.62	72.34
	3703.5	1	MD	−11.74	−3.78	26.98	101.40	48.72
		2	MD	−11.86	−4.24	26.50	100.90	51.60
		3	MD	−12.70	−4.04	26.70	99.28	50.36
		4	Ank	−13.26	−10.02	20.53	95.18	95.72
	3731.8	1	S-FD	−15.30	−6.71	23.94	92.62	68.44
		2	S-FD	−15.38	−5.62	25.08	93.02	60.66

Table 4. *Cont.*

Strata	Depth (m)	Measured Point	Cement Types	$\delta^{13}C_{PDB}$ (‰)	$\delta^{18}O_{PDB}$ (‰)	$\delta^{18}O_{SMOW}$ (‰)	Z	Paleo-Temperature (°C)
E_2e	3755.8	1	MD	−16.72	−2.72	28.06	91.72	42.40
		2	MD	−21.42	−2.26	28.54	82.32	39.76
		3	MD	−20.54	−2.66	28.14	83.94	42.06
		4	MD	−16.98	−3.28	27.50	90.92	45.68

Abbreviations: MD: micritic dolomite, S-FD: silt-to-fine crystalline dolomite, CCD: coarse crystalline dolomite, Ank: ankerite.

Table 5. Bulk Rock Carbon and Oxygen Isotope Test Data of Calcareous Sandstone in the Zhuhai and Enping Formations in Panyu A Sag.

Strata	Well Name	Depth (m)	$\delta^{13}C_{PDB}$ (‰)	$\delta^{18}O_{PDB}$ (‰)	$\delta^{18}O_{SMOW}$ (‰)	Z	Paleo-Temperature (°C)
E_3z	PY10F	3371.6	−9.98	−12.4	18.08	100.69	120.07
	PY10A	3530	−9.98	−12.88	17.58	100.45	125.56
	PY10A	3418.5	−10.61	−12.76	17.71	99.22	124.20
	PY10A	3424.17	−10.11	−13.1	17.36	100.07	128.21
E_2e	PY10A	3686	−11.41	−8.66	21.93	99.62	83.72
	PY10A	3710.3	−11.01	−10.4	20.14	99.57	99.31
	PY10D	3604	−10.14	−10.94	19.58	101.09	104.57
	PY10 D	3631.47	−10.94	−8.15	22.46	100.84	79.52
	PY10 D	3796.44	−9.79	−8.26	22.35	103.14	80.41
	PY10 D	3798.39	−9.75	−8.36	22.24	103.17	81.23
	PY10 D	3799.13	−10.1	−9.24	21.34	102.01	88.70

4.4. Displacement Pressure and Breakthrough Pressure

Three calciferous sandstone samples and 11 reservoir samples were selected for high-pressure mercury injection tests. The measured displacement pressures of the samples are shown in Table 6. The displacement pressure of calciferous sandstone ranges from 0.779 MPa to 1.417 MPa, with an average of 1.013 MPa, while that of the sandstone reservoir ranges from 0.035 MPa to 0.901 MPa, with an average of 0.275 MPa. The displacement pressure difference in the reservoir–seal assemblage composed of sandstone and calciferous sandstone is 0.738 MPa. The breakthrough pressure of calciferous sandstone measured using the pulse decay method is 0.5 MPa, and that of mudstone is 1.6 MPa (Figure 6).

Table 6. Displacement pressure data of calcareous sandstone and sandstone reservoirs in the Zhuhai–Enping Formations in Panyu A Sag.

Well Name	Depth (m)	Lithology	Porosity (%)	Permeability (mD)	Displacement Pressure (MPa)	Ave. Displacement Pressure (MPa)
PY10-A	3530	Calcareous sandstone	8.371	0.263	0.842	1.013
	3686	Calcareous sandstone	4.828	0.0431	1.417	
PY10-D	3604	Calcareous sandstone	9.992	0.127	0.779	
PY10-A	3710.3	Sandstone reservoirs	10.9	2.56	0.163	0.275
	3671.80	Sandstone reservoirs	14.5	4.69	0.749	
	3690.93	Sandstone reservoirs	9.5	3.26	0.901	
	3712.94	Sandstone reservoirs	19.4	14.7	0.242	
	3726.00	Sandstone reservoirs	14.2	/	0.040	
	3738.00	Sandstone reservoirs	17.1	30.7	0.174	

Table 6. *Cont.*

Well Name	Depth (m)	Lithology	Porosity (%)	Permeability (mD)	Displacement Pressure (MPa)	Ave. Displacement Pressure (MPa)
PY10-A	3758.13	Sandstone reservoirs	13.3	20.6	0.187	0.275
	3788.93	Sandstone reservoirs	10.9	9.77	0.330	
	3795.17	Sandstone reservoirs	14.9	837	0.035	
	3798.93	Sandstone reservoirs	12.5	117	0.091	
	3844.00	Sandstone reservoirs	11.3	67.7	0.114	

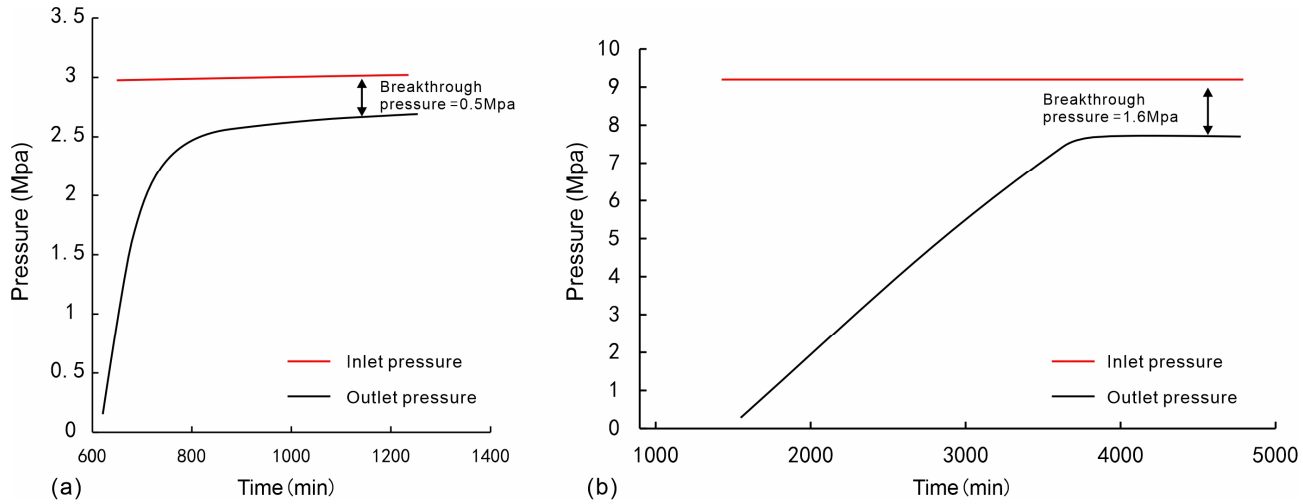

Figure 6. Measured breakthrough pressure for calcareous sandstone and mudstone cap rock in the Enping–Zhuhai Formations, Panyu A Sag. (**a**) PY10-D, 3564.91 m, calcareous sandstone; (**b**) PY10-D, 3816.91 m, mudstone.

5. Discussion

5.1. Genetic Mechanisms and Development Models of Calcareous Sandstones

5.1.1. Local Marine Transgressions

Since the Late Eocene (33 Ma), the Pearl River Mouth Basin has occupied a central position within a composite continental margin magmatic arc. Influenced by differential crustal thinning, the South China Sea region experienced subduction of the Paleo-South China Sea and rifting of the Neo-South China Sea Basin [37–40]. This differential thinning not only redistributed crustal thickness but also triggered terrace-style basin subsidence, driving progressive marine transgressions. Consequently, the formation of the South China Sea exhibits characteristics of a gradual marginal sea tectonic cycle [40]. Following the rifting of the Neo-South China Sea, marine transgressions advanced progressively across the northern South China Sea from south to north, as well as east to west during the period from 38 Ma to 23 Ma [39].

During the Oligocene, terrigenous detritus was transported via submarine channels to the Baiyun Sag, with the marine transgression progressively extending westward into the Zhu I Depression [41]. Following the interpretation of seismic data and the application of decompaction correction [42,43], the original sedimentary stratigraphic thicknesses for the Early and Late Enping stages were derived. Subsequent reconstruction of the paleotopography for different periods was achieved through 3D visualization employing the "template method." (Figure 7). Paleogeomorphic reconstructions of the Enping period reveal that seawater advanced northward through a conduit between the Dongsha Uplift and Xi'en Low Uplift, entering the southern subsag of Panyu A Sag (Figure 7). This hydrodynamic regime provided essential conditions for the formation of marine-influenced

calcareous sandstones and thin mudstones within deep sand-rich strata of the Panyu A Sag. In the northern area of Panyu A Sag, the topographically higher terrains of Wells PY10-D and PY10-F contrast with the lower-lying area of Well PY10-A in the southern area. This paleogeomorphic configuration resulted in more frequent marine incursions into the PY10-A area, while shallower water depths across the PY10-D and PY10-F areas.

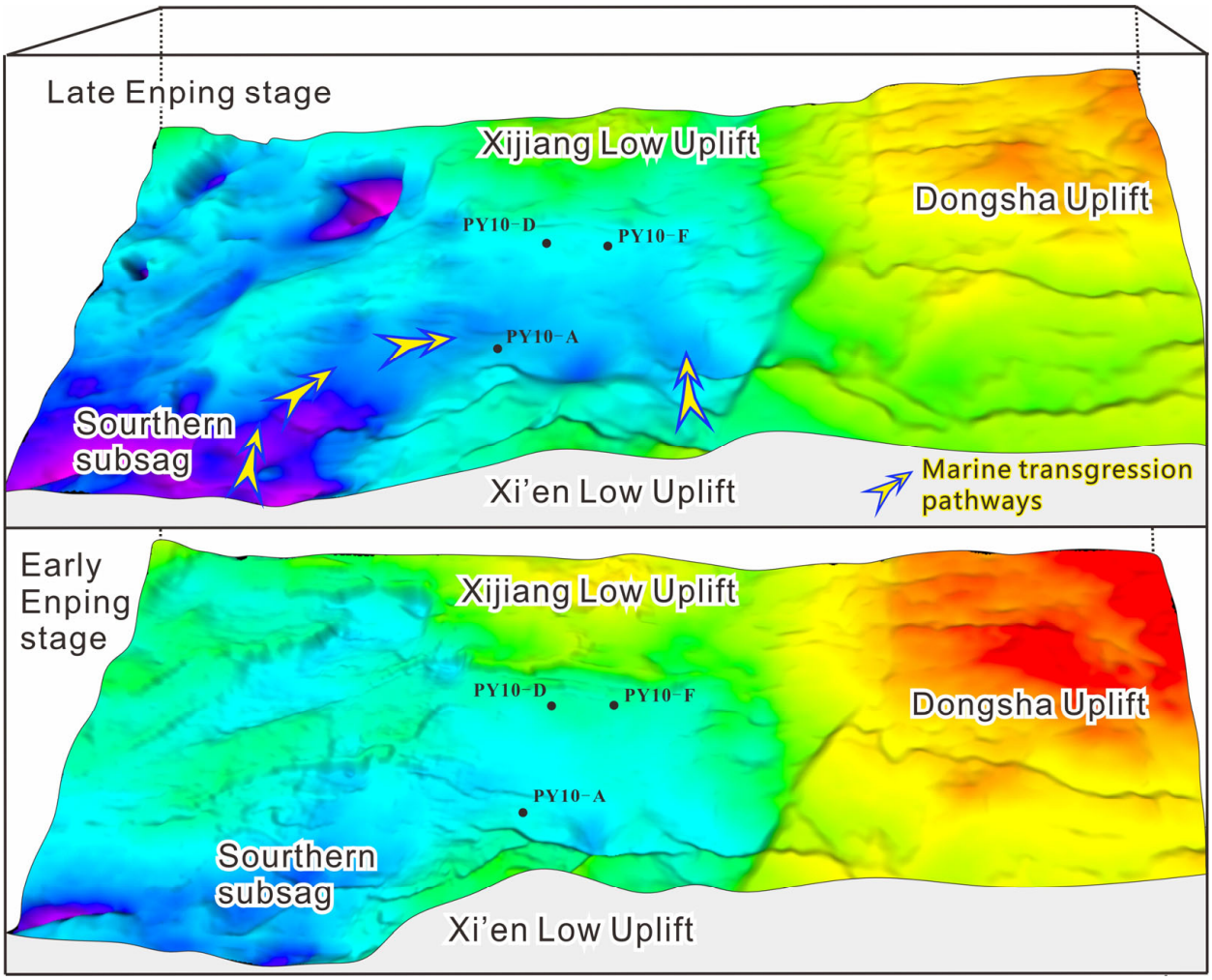

Figure 7. Restored paleogeomorphology of Panyu A Sag during the Enping depositional stage, the arrows indicate the marine transgression pathways.

In the study area, the glauconite within the calcareous sandstone is well-preserved in morphology and shows no signs of plastic deformation, indicating minimal transport and an authigenic origin [44]. Some glauconite grains have been subsequently replaced by dolomite (Figure 3c). A variety of bioclasts are observed under the microscope, coexisting with detrital grains (Figure 3d–i), suggesting relatively strong wave action capable of transporting bioclasts to the shallow-water depositional area [45]. Furthermore, the major element oxides CaO, MgO, and Fe_2O_3 (particularly MgO) from well PY10-A show three distinct peaks within the upper member of the Enping Formation (Table 1 and Figure 8), indicating three large-scale marine transgression events in this region [46].

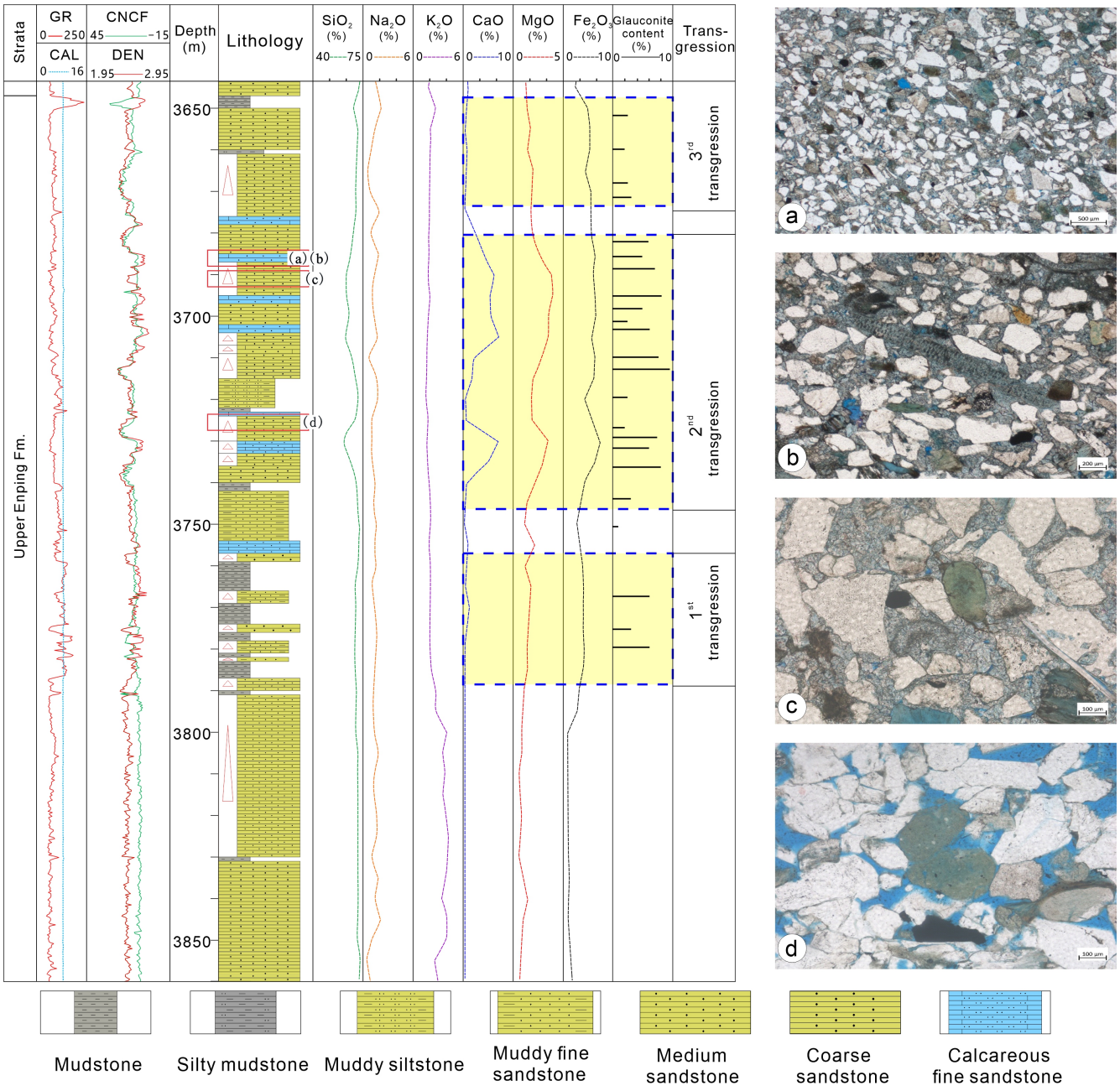

Figure 8. Major element data profile of the Enping Formation in Well PY10-A, Panyu A Sag. (**a**) Ankerite exhibiting basal cementation, E_2e, Well PY10-A, 3686 m, blue epoxy-impregnated, PPL; (**b**) Echinoderm bioclasts replaced by ankerite, E_2e, Well PY10-A, 3686 m, blue epoxy, PPL; (**c**) Scattered elliptical green glauconite grains, E_2e, Well PY10-A, 3690.93 m, blue epoxy, PPL; (**d**) Minor elliptical glauconite particles, E_2e, Well PY10-A, 3726 m, blue epoxy, PPL. PPL: plane-polarized light.

Trace elements and their concentrations in sedimentary rocks exhibit high sensitivity to variations in aqueous media within depositional environments, providing robust proxies for reconstructing paleoenvironmental and paleoclimatic evolution [47,48]. This study employs Sr/Cu, B/Ga, and V/(V + Ni) ratios to investigate paleoenvironmental changes, with trace element analytical results presented in Tables 2 and 3 and Figure 9. Well PY10-A in the study area exhibits Sr/Cu ratios predominantly exceeding 5 during the depositional period of the Zhuhai–Enping formations (Figure 9a), indicating a prevailing relatively dry and hot climatic condition. The B/Ga ratio serves as a reliable proxy for paleosalinity reconstruction [49]. Analytical results demonstrate that the Enping Formation predominantly

records freshwater to brackish conditions, while the Zhuhai Formation transitions into brackish to saline environments (Figure 9b,e). Both units are interpreted as nearshore depositional settings with intermittent marine influences. Particularly during the late Enping depositional stage, the south-to-north transgression advance resulted in more pronounced marine influence at Well PY10-A in the southern area of Panyu A Sag, leading to elevated salinity levels. Overall, the water column remained poorly stratified, developing anaerobic to sub-reductive conditions that facilitated organic matter preservation and early diagenetic cementation. The data of Well PY10-A exhibits frequent fluctuations in paleoclimatic and paleosalinity conditions. This cyclic variation in hydrological parameters created a unique geochemical environment conducive to dolomite diagenesis. Kinetic modeling reveals that pulsed injections of terrestrial freshwater into marine systems trigger oscillatory variations in ionic activities (e.g., Ca^{2+}, Mg^{2+}) within the water column. Paradoxically, such metastable saturation states facilitate sustained growth of dolomite crystal nuclei [50–52].

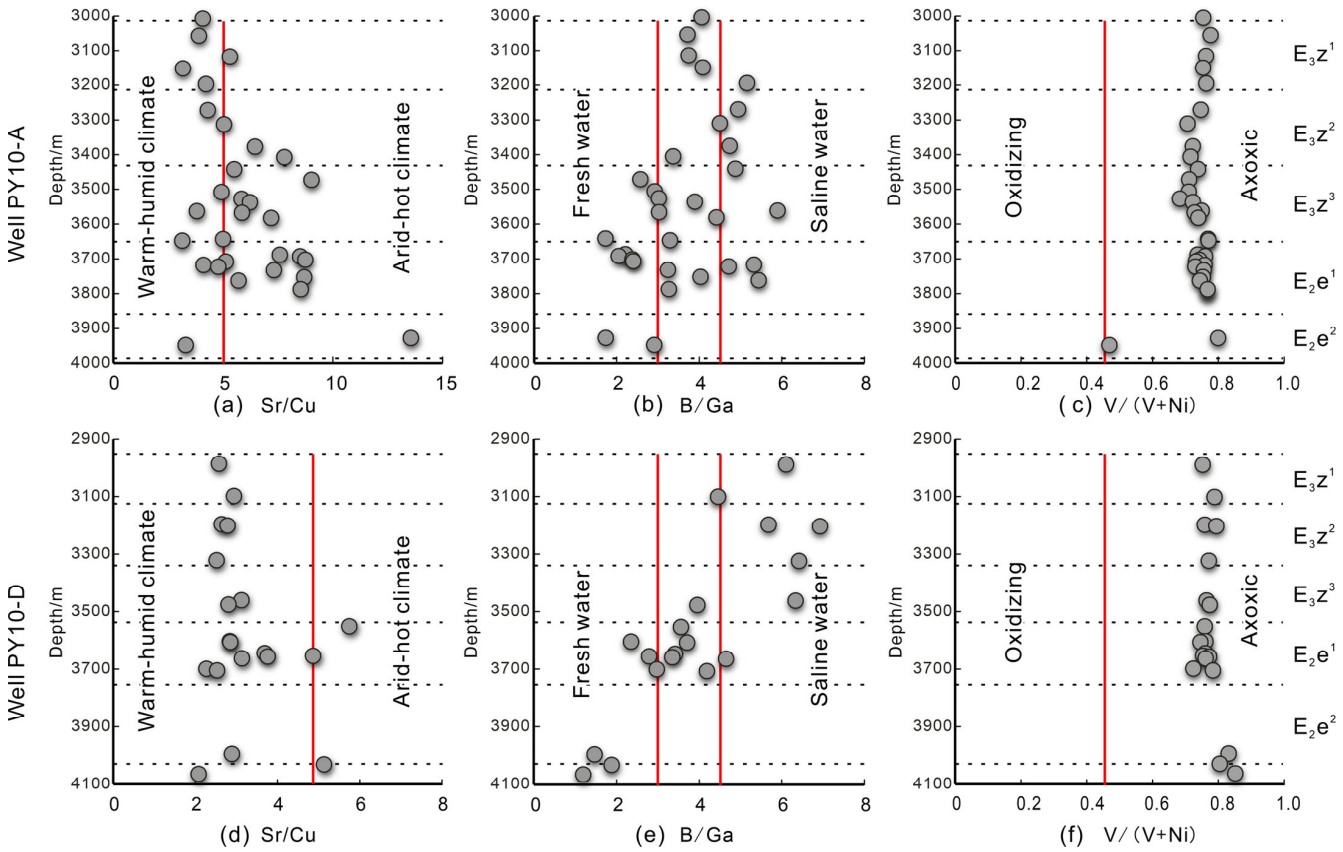

Figure 9. Trace element ratio plots vs. depth for Wells PY10-A and PY10-D in the Panyu A Sag. (**a**) Sr/Cu ratio vs. depth, (**b**) B/Ga ratio vs. depth, (**c**) V/(V + Ni) ratio vs. depth for Well PY 10-A and (**d**) Sr/Cu ratio vs. depth, (**e**) B/Ga ratio vs. depth, (**f**) V/(V + Ni) ratio vs. depth for Well PY 10-D.

5.1.2. Burial Diagenesis

Controls of Burial Diagenesis on Dolomite/Ankerite Cementation

Carbon and oxygen isotope data are often used to explain the genesis of dolomite. The carbon and oxygen isotope compositions of dolomite are mainly controlled by the carbon and oxygen isotope compositions of the dolomitized minerals and by the salinity and temperature of the diagenetic fluids [53–55].

(1) Paleosalinity

Keith and Weber combined $\delta^{13}C$ and $\delta^{18}O$ to propose an empirical formula for distinguishing marine from freshwater carbonate rocks [56]. This formula calculates a dimensionless Z-value to determine the nature of the aqueous medium and indicate paleosalinity.

$$Z = 2.048 \times (\delta^{13}C + 50) + 0.498 \times (\delta^{18}O + 50) \quad (1)$$

In the formula, $\delta^{13}C$ and $\delta^{18}O$ values are both referenced to PDB standard. The Z-value larger than 120 indicates a marine (seawater-derived) aqueous medium, while the Z-value less than 120 indicates a terrestrial freshwater-derived aqueous medium.

Based on the calculated Z-values (Tables 4 and 5), the dolomite samples from the Zhuhai Formation exhibit Z-values ranging from 80.632 to 101.471, while those from the Enping Formation range from 82.318 to 101.392. All Z-values are below 120, indicating that the carbonate cements in these samples formed in a freshwater-dominated environment.

Research by Irwin et al. demonstrates that during diagenesis, the carbon and oxygen isotopic compositions of CO_2 generated at different stages vary significantly: ① 0–10 m depth: Bacterial sulfate reduction produces CO_2 with $\delta^{13}C_{PDB}$ value is −25‰ and $\delta^{18}O_{PDB}$ values range from 0‰ to −2‰; ② 10–1000 m depth: Bacterial fermentation yields CO_2 with $\delta^{13}C_{PDB}$ value is +15‰ and $\delta^{18}O_{PDB}$ values range from −1.5‰ to −5‰; ③ >1000 m depth: Organic acids from kerogen degradation contribute to CO_2 with $\delta^{13}C_{PDB}$ value is −20‰ and $\delta^{18}O_{PDB}$ values range from −3.5‰ to −7‰ [57]. The carbon and oxygen isotopic composition distribution diagram of carbonate cements (Figure 10a) reveals that the calcareous sandstone cements in the Zhuhai–Enping Formations of Panyu A Sag, predominantly interpreted as diagenetic carbonates formed during burial processes. A subset of data points clusters in Zone III, attributed to carbonate precipitated associated with organic acid decarboxylation.

(2) Paleotemperature

Water temperature is a critical factor controlling the stable isotopic composition of carbonate rocks. Temperature exerts a far greater influence on $\delta^{18}O$ values than salinity, while $\delta^{13}C$ values show minimal variation with temperature. Consequently, $\delta^{18}O$ can serve as a reliable indicator of paleotemperature when salinity remains constant [58]. Numerous scholars have proposed using $\delta^{18}O$ to determine paleotemperatures [56,58–60]:

$$1000\ln\alpha_{\text{dolomite-water}} = 2.73 \times 10^6 T^{-2} + 0.26 \quad (2)$$

In the formula, αdol-w = $(1 + (\delta^{18}O_{dol}/1000))/(1 + (\delta^{18}O_w/1000))$, T is temperature in Kelvin (K), $\delta^{18}O_{SMOW} = 1.03086 \times \delta^{18}O_{PDB} + 30.86$ (Converts PDB-standard values to SMOW), assume $\delta^{18}O_{SMOW}$ of modern seawater is 0‰.

In situ oxygen isotope thermometry results indicate that carbonate cements formed at temperatures ranging from 39.76 °C to 95.71 °C (Table 4). In the study area, micritic, silt-crystalline, and fine-crystalline dolomites primarily formed under the influence of diagenetic processes, while coarse-crystalline dolomites and ankerites were partially influenced by organic acid activity (Figure 10a). Dolomite types correspond to distinct developmental stages, with three phases identified. Micritic dolomite formed at 39.76–51.59 °C, representing the eodiagenesis A stage (shallow burial). Silt-fine crystalline dolomite formed at 60.66–72.64 °C, representing the eodiagenesis B stage (moderate burial). Coarse-crystalline & ankerite formed at 79.51–128.21 °C, representing the mesodiagenesis A stage (deep burial) (Figure 10b).

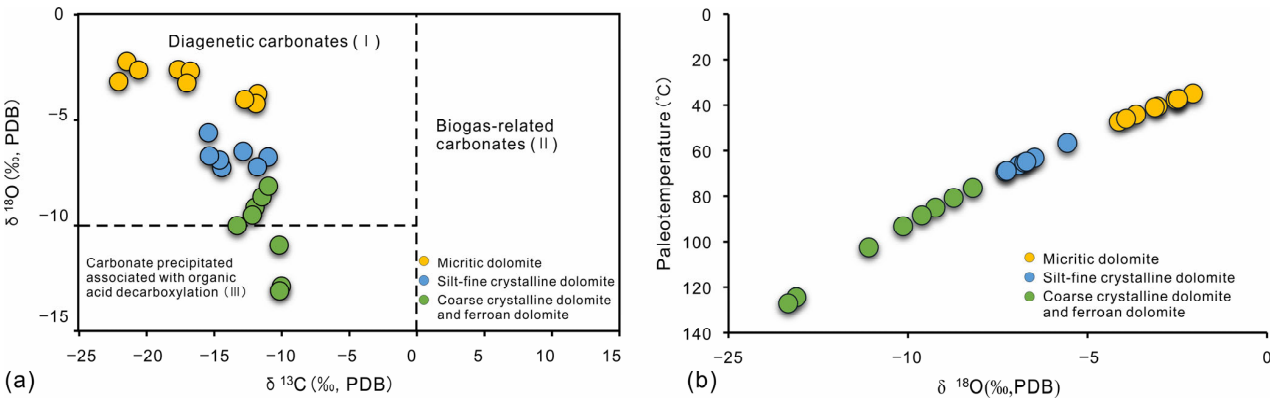

Figure 10. Characteristics of carbon and oxygen isotopic composition in the PY A Sag. (**a**) Carbon and oxygen isotopic composition of different dolomite types; (**b**) Relationship between oxygen isotopes and paleotemperature.

As rock burial depth increases, bacterial activity diminishes, and organic acid decarboxylation driven by thermal catalysis becomes the dominant reaction, generating hydrocarbons and CO_2. This CO_2 can migrate into reservoirs prior to or concurrently with hydrocarbon migration, leading to elevated CO_2 pressure within the diagenetic system and subsequent precipitation as carbonate minerals [61]. Organic acids undergo decarboxylation to produce CO_2, which combines with water to form carbonic acid (H_2CO_3). Subsequent ionization generates ions such as H^+, HCO_3^-, and CO_3^{2-} [62]. Simultaneously, organic acids dissolve feldspar or early-stage bioclasts, and the transformation of certain clay minerals releases Ca^{2+} ions. When these HCO_3^- and CO_3^{2-} ions encounter Ca^{2+} (or Mg^{2+}/Fe^{2+}) in pore water, they precipitate as ferroan calcite or ankerite [63]. Under the microscope, moldic pores formed by feldspar dissolution can be observed, along with intergranular medium-to-coarse crystalline ankerite spatially associated with feldspar dissolution (Figure 4k).

Controls of Burial Diagenesis on Gypsum/Anhydrite Dolomite Cementation

The ratios of Rb/Zr, Zr/Y, and Yb/La can be used to reflect changes in water depth related to sea-level fluctuations. The Rb/Zr ratio serves as an effective indicator of water depth and hydrodynamic conditions. A higher Rb/Zr value indicates deeper water and weaker hydrodynamic energy [64]. The Zr/Y ratio provides insights into sediment provenance distance and water depth. A lower Zr/Y value suggests a depositional environment farther from the terrigenous source and characterized by deeper seawater [65]. The Yb/La ratio is effective in identifying variations in water depth. In shallow marine settings, seawater is typically enriched in light rare earth elements (e.g., La), whereas deep marine environments are relatively enriched in heavy rare earth elements (e.g., Yb). Thus, a higher Yb/La value indicates deeper water [66]. As shown in Figure 11, well PY10-D in the northern area has Yb/La values <0.075, while well PY10-A in the southern area exhibits Yb/La values consistently >0.075. This indicates shallower water depths in the northern area compared to the south, resulting in stronger evaporation and relatively more developed gypsum deposits.

Overall, during the depositional period of the Zhuhai–Enping Formation in the study area, the environment was characterized by a relatively dry and hot freshwater to brackish nearshore setting, with occasional saline water incursions. This represented an anaerobic to sub-reducing environment with weak water stratification. When the climate shifted to semi-arid or arid conditions, continuous evaporation concentrated the depositional water body until $CaSO_4$ reached supersaturation, leading to the precipitation of gypsum

($CaSO_4 \cdot H_2O$). Geomorphologically, Wells PY10-D and PY10-F in the northern area are topographically higher than Well PY10-6A in the southern area (Figure 7). Consequently, the northern area exhibits shallower water depths, stronger evaporation, and more extensive gypsum development.

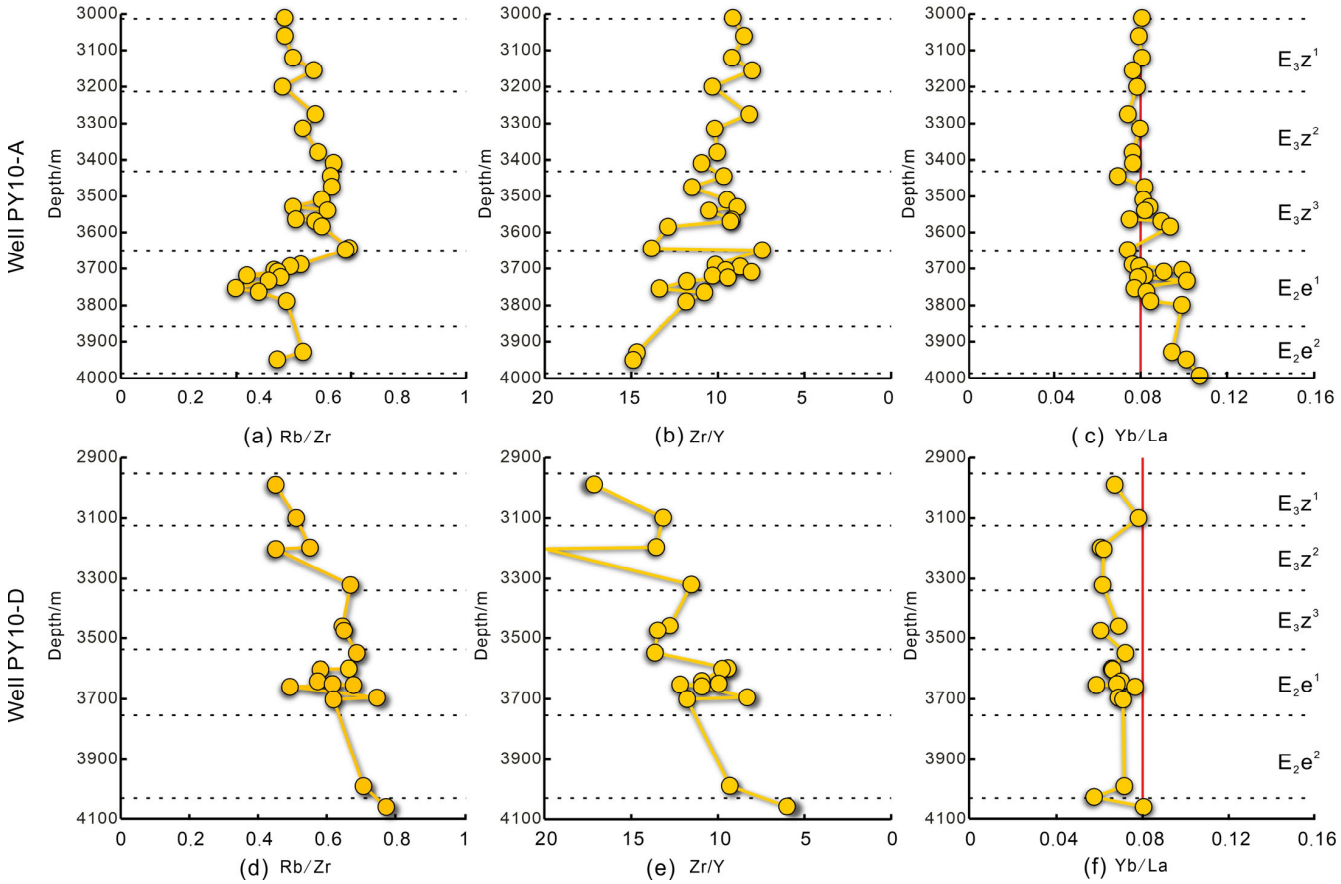

Figure 11. Rare earth element ratio plots vs. depth for Wells PY10-A and PY10-D in the Panyu A Sag. (**a**) Rb/Zr ratio vs. depth, (**b**) Zr/Y ratio vs. depth, (**c**) Yb/La ratio vs. depth for Well PY 10-A and (**d**) Rb/Zr ratio vs. depth, (**e**) Zr/Y ratio vs. depth, (**f**) Yb/La ratio vs. depth for Well PY 10-D.

5.2. Development Model of Calcareous Sandstones

Based on the transgression background, developmental characteristics, genetic mechanisms, and diagenetic evolution of calcareous sandstones, a development model for calcareous sandstones of the Zhuhai–Enping Formations in the Panyu A Sag has been established (Figure 12).

During the depositional period, marine transgression events reduced sedimentation rates, facilitating the enrichment of bioclastic materials while providing abundant sources of Ca^{2+} and Mg^{2+}. Local intermittent transgressions caused dolomite saturation states to oscillate between supersaturation and undersaturation, promoting dolomite formation. In the syndiagenetic to early diagenetic stages, seawater evaporation led to supersaturation of SO_4^{2-} and Ca^{2+}, precipitating gypsum/anhydrite. Simultaneously, supersaturated Ca^{2+} and Mg^{2+} formed early-stage calcite/dolomite. Upon reaching the mesodiagenetic stage, increasing burial depth activated two key carbon sources for carbonate cementation: sulfate reduction and thermal decarboxylation of organic acids. As organic acids became progressively depleted, the diagenetic environment shifted from acidic to alkaline. Concurrently, the transformation of smectite to illite released Fe^{3+} and Mg^{2+}. This triggered dolomitization of calcite and subsequent formation of ankerite, ultimately resulting in dense sandstone cementation (Figure 12).

During the late Enping period, carbon and oxygen isotope analyses combined with elemental data indicate episodic sea-level rise, leading to water salinization that transitioned the freshwater lake basin into a brackish lacustrine environment. This shift provided the depositional setting essential for calcareous sandstone formation. In the Panyu A Sag along the sag margin, Wells PY10-D and PY10-F developed significant anhydrite deposits due to shallow water depths and intense evaporation. In contrast, Well PY10-A in the southern area experienced seawater incursions that delivered abundant ions, promoting dolomite cementation. Following the transition from continental to marine deposition in the Zhuhai Formation, sustained ion supply coupled with increasing burial depth triggered recrystallization of dolomite, forming anhedral coarse-crystalline (ferroan) dolomite (Figure 12).

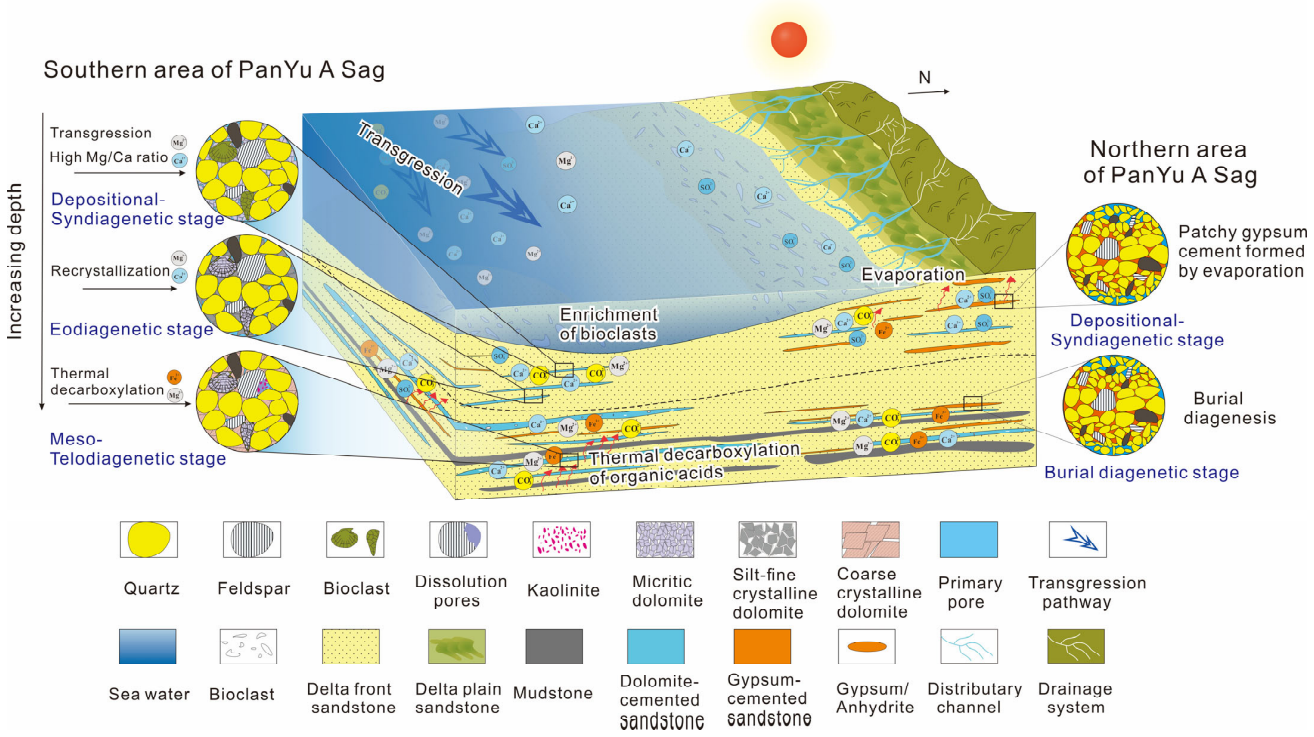

Figure 12. Development model diagram of calcareous sandstones in the Enping–Zhuhai Formations, Panyu A Sag.

5.3. Sealing Mechanisms of Calcareous Sandstones

5.3.1. Sealing Mechanism and Effectiveness Evaluation of Calcareous Sandstones

Hydrocarbon exploration practices demonstrate that calcareous sandstones within the sand-rich sequences of the Zhuhai–Enping Formations in the Panyu A Sag play a critical role as caprocks for hydrocarbon accumulation [21]. The sealing capacity primarily relies on the displacement pressure differential between the caprock and reservoir [67–69]. Thus, higher displacement pressure in the caprock correlates with stronger capillary pressure sealing capability, whereas lower pressure results in weaker sealing. This stu dy statistically analyzes displacement pressures of calcareous sandstone caprocks and reservoirs across the research area, calculating the maximum hydrocarbon column height sealed by the caprocks. The results confirm the effectiveness of calcareous sandstones as sealing layers.

The maximum hydrocarbon column height (H) sealed by a caprock occurs when buoyancy equals the displacement pressure difference between the caprock and reservoir. The calculation formula is given by [70]:

$$H = (Pcap - Pres)/((Pw - Pg) * g) \quad (3)$$

In the formula, H = Hydrocarbon column height ($\times 10^3$ m); $Pcap$ = Displacement pressure of the caprock (MPa); $Pres$ = Displacement pressure of the reservoir (MPa); ρw = Formation water density (typically 1.0×10^3 kg/m^3); ρg = Hydrocarbon density (typically 0.75×10^3 kg/m^3); g = Gravitational acceleration (9.8 m/s^2).

This study reveals that the displacement pressure differential between calcareous sandstone and sandstone reservoir is 0.738 MPa (Table 6). With calcareous sandstone caprock permeability < 0.3 mD, the average sealed hydrocarbon column height calculated directly from constant-rate mercury injection data reaches 295.2 m. Analysis of displacement pressures via pulse-decay breakthrough pressure tests (Figure 6) and constant-rate mercury injection experiments demonstrates that 2–3 m thick transgressive calcareous sandstone layers can seal oil columns of 234–520 m (Figure 13), confirming their effectiveness as caprocks. The average oil column height sealed by calcareous sandstones of all Upper Enping Formation is 437.90 m. In contrast, mudstone caprocks in the study area exhibit higher breakthrough pressures (predominantly 1.6 MPa; Figure 6b), with a calculated maximum hydrocarbon column height of 640 m, indicating superior sealing capacity compared to calcareous sandstones.

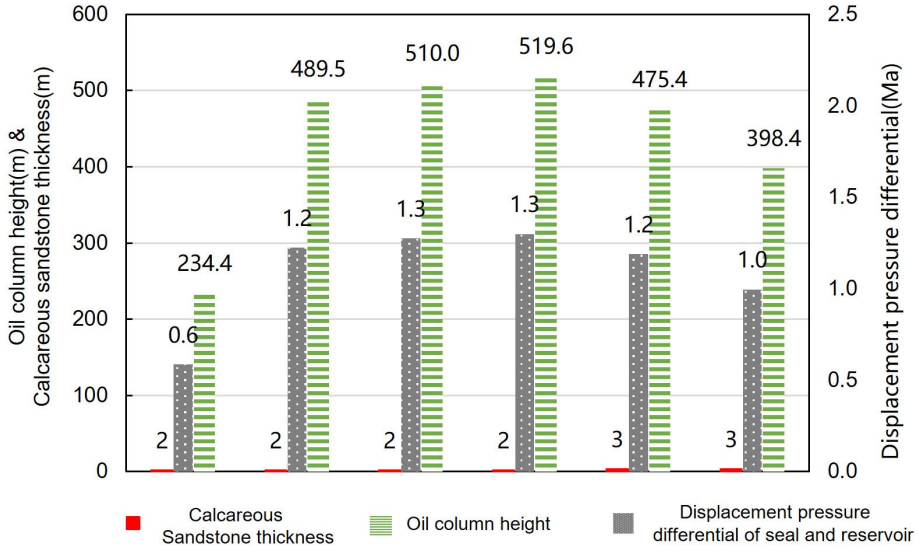

Figure 13. Distribution histogram of calcareous sandstone thickness and cap rock capacity in the Enping–Zhuhai Formations, Panyu A Sag.

5.3.2. Development Model of Hydrocarbon Accumulation

(1) Reservoir–seal assemblage pattern

During the middle depositional stage of the Enping Formation, the lake basin in the study area expanded rapidly, reaching its maximum extent and forming a maximum flooding surface (MFS) (Figure 14). This period developed a regionally extensive mudstone layer with a thickness of 28 m, serving as the most critical regional seal. In the late Enping period, the lake basin shrank and experienced intermittent marine transgressions, leading to localized water salinization. This resulted in the deposition of interbedded calcareous sandstone, mudstone, and normal sandstone. The upper section of the Enping Formation has a thickness of 211–213 m and a sandstone content of 78.1%–86.8%. The lithology is predominantly composed of medium- to fine-grained sandstone, calcareous sandstone, and mudstone. Sandstones from the braided river delta plain or braided river delta front subfacies are interbedded with lacustrine (marine) flooding mudstones and calcareous sandstones, forming two types of high-quality reservoir–seal assemblages (Figure 14).

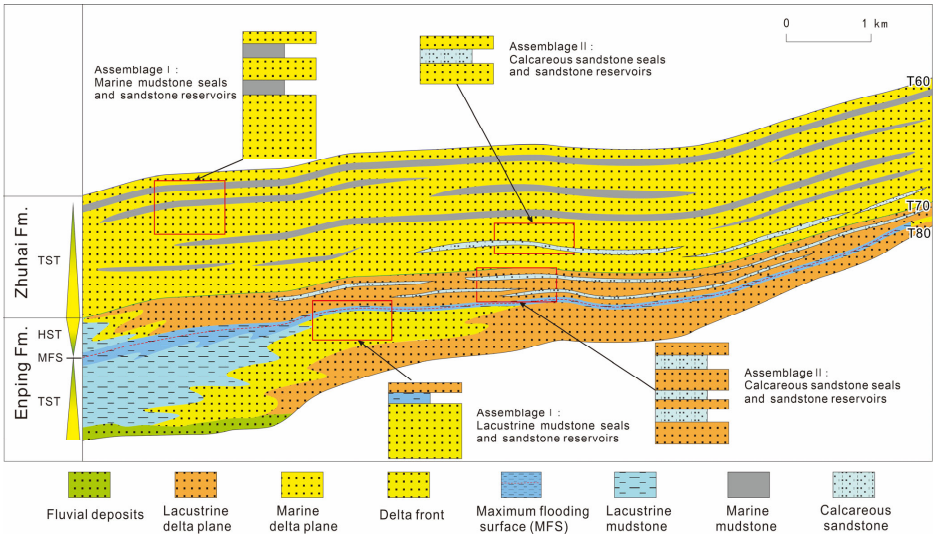

Figure 14. Development model diagram of reservoir–seal assemblage in the Enping–Zhuhai Formations, Panyu A Sag.

(2) Hydrocarbon accumulation model

The Panyu A Sag exhibits a hydrocarbon accumulation model characterized by "fault-efficient migration and near-source dominant accumulation" [21]. Long-active trap-controlling faults extensively connect with high-quality source rocks of Wenchang Formation in the southern subsag. Hydrocarbons migrate along these faults into braided river delta sandstone reservoirs of the Enping and Zhuhai Formations, ultimately accumulating in fault-block traps with favorable lateral sealing capacity under the effective confinement of lacustrine flooding mudstones and calcareous sandstones. The reservoirs feature large-scale efficient charging and multi-strata accumulation. Overall, efficient hydrocarbon preservation and enrichment are controlled by vertically interbedded tight calcareous sandstones with strong cementation (formed by intermittent marine transgressions superimposed with burial diagenesis) and thin marine transgressive mudstones (Figure 15).

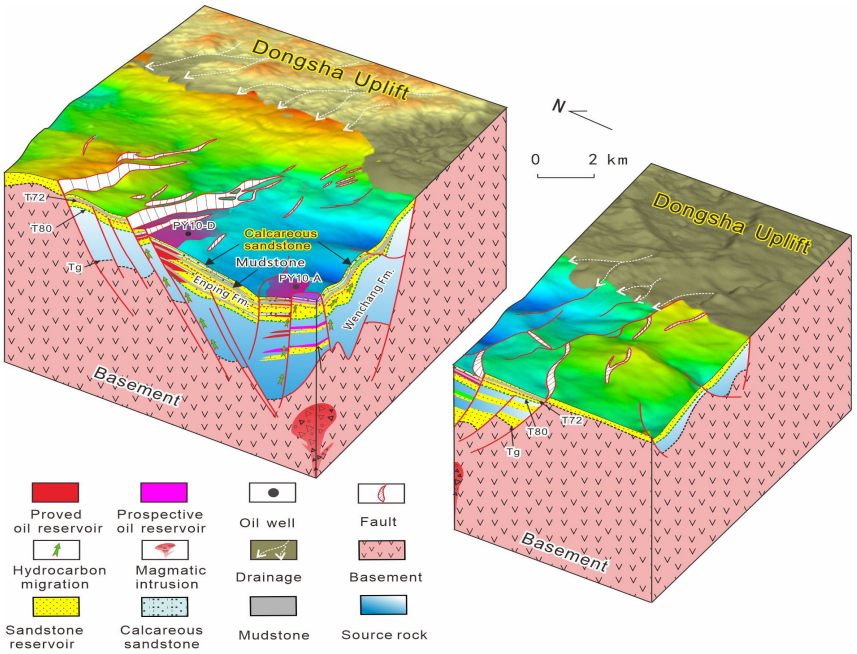

Figure 15. Development model diagram of hydrocarbon accumulation controlled by calcareous sandstone-thin mudstone interbeds in the PY A Sag (Modified from [21]).

6. Conclusions

(1) The calcareous sandstone cements in the Zhuhai–Enping formations of the Panyu A Sag are mainly composed of dolomite, ankerite, and anhydrite. Anhydrite typically fills large intergranular pores and forms polkilotopic cement between grains. With increasing burial depth, dolomite transitions from micritic dolomite to silt-sized and fine-crystalline dolomite, and finally to coarse-crystalline dolomite.

(2) The expansion of the New South China Sea at 33 Ma during the late Eocene led to a local transgression, which provided ions such as Ca^{2+} and Mg^{2+}, forming the material basis for early dolomite formation. As burial depth increased, organic acids were gradually depleted, and the diagenetic environment shifted from acidic to alkaline, leading to the dolomitization of early-formed calcite and the formation of ankerite. In the northern part of the study area, under strong evaporation conditions, the supersaturation of SO_4^{2-} and Ca^{2+} concentrations resulted in the precipitation of gypsum/anhydrite.

(3) The braided river delta distributary channel sandstones, together with lacustrine (marine) flooding mudstones and calcareous sandstones, form two types of high-quality reservoir–seal combinations. Vertically interbedded tight calcareous sandstones and thin marine transgressive mudstones collectively control efficient hydrocarbon preservation and enrichment.

Author Contributions: Conceptualization and methodology, Y.Z.; software, K.W. and W.Z.; formal analysis, K.W.; investigation, Y.Z.; resources, G.P., X.Q. (Xinwei Qiu) and Z.L.; data curation, W.Z.; writing—original draft preparation, K.W.; writing—review and editing, Y.Z.; visualization, W.Z.; supervision, X.Q. (Xiaoming Que) and P.J.; funding acquisition, G.P. All authors have read and agreed to the published version of the manuscript.

Funding: This research was funded by the National Natural Science Foundation of China (42472178) and the National Key R&D Program of China (2024YFE0114000).

Data Availability Statement: All of the data and models generated or used in the present study are available from the corresponding author upon request.

Acknowledgments: The authors would like to express their sincere thanks to the Shenzhen Branch of CNOOC (China) Limited for their assistance in providing the data, and for their technical input to this work.

Conflicts of Interest: Authors Guangrong Peng, Wenchi Zhang, Xinwei Qiu, Zhensheng Li, Xiaoming Que and Peimeng Jia are employed by the Shenzhen Branch of CNOOC (China) Limited. The remining authors declare that they have no known competing financial interest or personal relationships that might have influenced the work presented in this article.

Abbreviations

The following abbreviations are used in this manuscript:

PPL	Plane-polarized light
XPL	Cross-polarized light
SEM	Scanning electron microscope
MD	Micritic dolomite
S-FD	Silt-to-fine-crystalline dolomite
CCD	Coarse-crystalline dolomite
An	Ankerite
Gp	Gypsum

References

1. Liao, M.G.; Huang, Z.Q.; Liang, W.F.; Liao, J.J. Geological Characteristics and Genesis Analysis of Calcareous Intercalation Layer of Oil Group A in N Oilfield. *Sediment. Geol. Tethyan Geol.* **2020**, *40*, 26–34. (In Chinese)
2. Shang, F.K.; Zhang, K.H.; Shi, H.G.; Xu, Y.D.; Zhang, Y.J.; Chen, L. "Ternary composite" genesis and petroleum geological significance of calcareous barriers in the 1st sand group of Shawan-1 member of Neogene in the Chepaizi bulge of the Junggar Basin. *China Pet. Explor.* **2020**, *25*, 112–125. (In Chinese)
3. Curtis, C.D. Possible links between sandstone diagenesis and depth-related geochemical reactions occurring in enclosing mudstones. *J. Geol. Soc.* **1978**, *135*, 107–117. [CrossRef]
4. Surdam, R.C.; Crossey, L.J.; Hagen, E.S.; Heasler, H.P. Organic-Inorganic Interactions and Sandstone Diagenesis. *AAPG Bull.* **1989**, *73*, 1–23. [CrossRef]
5. Huang, S.J.; Shi, H.; Mao, X.D.; Zhang, M.; Shen, L.C.; Wu, W.H. Diagenetic alteration of earlier palaeozoic marine carbonate and preservation for the information of seawater. *J. Chengdu Univ. Technol. (Sci. Technol. Ed.)* **2003**, *30*, 9–18. (In Chinese)
6. Barnes, D.A.; Lundgren, C.E.; Longman, M.W. Sedimentology and Diagenesis of the St. Peter Sandstone, Central Michigan Basin, United States. *AAPG Bull.* **1992**, *76*, 1507–1532. [CrossRef]
7. Taylor, K.G.; Macquaker, J.H.S. Early diagenetic pyrite morphology in a mudstone-dominated succession: The Lower Jurassic Cleveland Ironstone Formation, eastern England. *Sediment. Geol.* **2000**, *131*, 77–86. [CrossRef]
8. Lynch, F.L. Mineral/Water Interaction, Fluid Flow, and Frio Sandstone Diagenesis: Evidence from the Rocks. *AAPG Bull.* **1997**, *80*, 486–504.
9. Rlykke, K.O.B.O. Fluid-flow processes and diagenesis in sedimentary basins. *Geol. Soc. Lond. Spec. Publ.* **1994**, *78*, 127–140.
10. Tan, X.F.; Jiang, W.; Wu, K.J.; Wang, H.; Xu, T.K.; Chen, S.J.; Ran, T. Sedimentation mechanism and petroleum significance of calcareous cements in continental clastic rocks: Comparison between the Kongdian Formation in the Jiyang Depression and the Xujiahe Formation in the western Sichuan Basin. *Pet. Geol. Exp.* **2016**, *38*, 293–302. (In Chinese)
11. Liu, H.N.; Deng, L.L.; Gong, Y.C.; Sun, W. Carbonate cement from Xujiahe Sandstone and its forming mechanism, West Sichuan Depression. *Nat. Gas Technol.* **2008**, *2*, 24–27. (In Chinese)
12. Zhang, Z.; Pang, J.; Yang, Y.T.; Cao, Y.H.; Qi, M.H.; Zhang, Y.Y.; Zhang, L.; Ma, S. Carbon and Oxygen isotope characteristics and genesis of carbonate cements in sandstone of the 4th Member of the Xujiahe Formation in the central western Sichuan depression, Sichuan basin, China. *Acta Geol. Sin.* **2022**, *96*, 2094–2106. (In Chinese)
13. Chowdhury, A.H.; Noble, J.A. Origin, distribution and significance of carbonate cements in the Albert Formation reservoir sandstones, New Brunswick, Canada. *Mar. Pet. Geol.* **1996**, *13*, 837–846. [CrossRef]
14. Lee, E.Y.; Kominz, M.; Reuning, L.; Gallagher, S.J.; Takayanagi, H.; Ishiwa, T.; Knierzinger, W.; Wagreich, M. Quantitative compaction trends of Miocene to Holocene carbonates off the west coast of Australia. *Aust. J. Earth Sci.* **2021**, *68*, 1149–1161. [CrossRef]
15. Han, X.F.; Liu, Z.B.; Li, Y.P.; Wen, J.T.; Wang, T. Genetic mechanism and controlling factors of calcareous sandstone of the Paleogene Shahejie Formation, Liaodong Gulf. *Pet. Geol. Recovery Effic.* **2018**, *25*, 65–71. (In Chinese)
16. Liu, D.L.; Shang, J.X.; Fu, T.; Ye, Q.; Kong, L.H. Influence research of calcareous intercalation on development effect in oil group ZJ1-5of Wenchang oilfield. *Pet. Geol. Eng.* **2015**, *29*, 73–75. (In Chinese)
17. Jiang, P.; Yang, C.Q.; Huang, G.Z.; Li, M.W. Study on Development Pattern of Zhujiang Formation Calcareous Sandstone in Wenchang Oilfield Group. *Spec. Oil Gas Reserv.* **2014**, *21*, 14–17. (In Chinese)
18. You, L.; Li, C.; Zhang, Y.Z. Distribution and Genetic Mechanism of Carbonate Cements in the Zhuhai Formation Reservoirs in Wenchang A Sag, Pear River Mouth Basin. *Oil Gas Geol.* **2012**, *33*, 883–889. (In Chinese)
19. Yuan, X.Q.; Yao, G.Q.; Yang, X.H. Constraints of Authigenic Clay Minerals on Deep Reservoirs in Wenchang A Sag. *Earth Sci.* **2019**, *44*, 909–918. (In Chinese)
20. Chang, S.Y.; Chen, D.X.; Wang, C.; Wang, Q.C.; Liu, Z.Y.; Wang, F.W. Preservation mechanism and model of primary pore diagenesis in deep reservoirs: Taking the Enping Formation and Wenchang Formation in the south of Huizhou Sag, Pearl River Mouth Basin as example. *J. Northeast Pet. Univ.* **2022**, *46*, 72–85. (In Chinese)
21. Xu, C.G.; Gao, Y.D.; Liu, J.; Peng, G.R.; Qiu, X.W.; Zhang, X.Z.; Jia, P.M. Major discoveries and significance of hydrocarbon exploration in the Paleogene reservoirs of Panyu A subsag, Xijiang sag, Pearl River Mouth Basin. *Acta Geol. Sin.* **2024**, *45*, 1031–1043. (In Chinese)
22. Peng, G.; Liu, P.; Song, P.; Gao, X.; Xiong, W.; Xiang, Q.; Han, B. Source rock attribute, oil classification and hydrocarbon accumulation main control factors of Xijiang main sag in Pearl River mouth Basin. *Earth Sci.* **2023**, *48*, 2361–2375. (In Chinese)
23. Zhao, Z.X.; Sun, Z.; Qiu, N.; Zhao, M.H.; Zhang, J.Z.; Li, F.C.; Lin, J.; Lee, E.Y. The paleo-lithospheric structure and rifting-magmatic processes of the northern South China Sea passive margin. *Gondwana Res.* **2023**, *120*, 162–174. [CrossRef]
24. Shi, H.S.; Shu, Y.; Du, J.Y. *Petroleum Geology of Paleogene in Pearl River Mouth Basin*; Geological Publishing House: Beijing, China, 2017. (In Chinese)

25. Pang, X.; Chen, C.M.; Shao, L.; Wang, C.S.; Zhu, M. Baiyun Movement, a great tectonic event on the Oligocene-Miocene boundary in the northern South China Sea and its implications. *Geol. Rev.* **2007**, *53*, 145–151. (In Chinese)
26. Shi, H.S.; Du, J.Y.; Mei, L.F.; Zhang, X.T.; Hao, S.H.; Liu, P.; Deng, P.; Zhang, Q. Huizhou movement and its significance in Pearl River Mouth Basin, China. *Pet. Explor. Dev.* **2020**, *47*, 447–461. (In Chinese) [CrossRef]
27. Gao, Y.D.; Liu, J.; Peng, G.R.; Chen, L.; Wang, Z.Y.; Shi, Y.L. New fields and resource potential of oil and gas exploration in Pearl River Mouth Basin. *Acta Pet. Sin.* **2024**, *45*, 183–201. (In Chinese)
28. Wu, Z.P.; Hu, Y.; Zhong, Z.H. Cenozoic faults characteristics and regional dynamic background of Panyu 4 sub-sag, Zhu I Dpression. *J. China Univ. Pet.* **2015**, *39*, 1–9. (In Chinese)
29. Zeng, Z.W.; Zhu, H.T.; Yang, X.H.; Xia, C.C.; Chen, Y.; Han, Y.C. Provenance transformation and sedimentary evolution of Enping Formation, Baiyun Sag, Pearl River Mouth Basin. *Earth Sci.* **2017**, *42*, 1936–1954. (In Chinese)
30. Zhang, W.W.; Liu, J.; Liu, L.H.; Zhang, X.Z.; Bai, H.J.; Yang, D.F. Lithology prediction technology and its application of Paleogene Wenchang Formation in Panyu 4 Depression, Pearl River Mouth Basin. *Lithol. Reserv.* **2022**, *34*, 118–125. (In Chinese)
31. Huang, S.J. *Diagenesis of Carbonate Rocks*; Geological Publishing House: Beijing, China, 2010. (In Chinese)
32. Zhou, H. Research on Petrological Characteristics and Diagenesis of the Lower Triassic Jialingjiang Formation in Libi Gorge of Chongqing Area, Eastern Sichuan Basin. Master's Thesis, Chengdu University of Technology, Chengdu, China, 2012. (In Chinese).
33. Jones, B.G. Dolomite Crystal Architecture: Genetic Implications for the Origin of the Tertiary Dolostones of the Cayman Islands. *J. Sediment. Res.* **2005**, *75*, 177–189. [CrossRef]
34. Nickel, E.H.; Grice, J.D. The IMA Commission on new minerals and mineral names: Procedures and guidelines on mineral nomenclature. *Mineral. Petrol.* **1998**, *64*, 237–263. [CrossRef]
35. You, X.L.; Jia, W.Q.; Xu, F.; Liu, Y. Mineralogical characteristics of ankerite and mechanisms of primary and secondary origins. *Earth Sci.* **2018**, *43*, 4046–4055. (In Chinese)
36. Wang, X.D. Favorable Main Controlling Factors of Paleogene Wenchang Formation in the Southwest of Huizhou Sag of Zhuyi Depression. Master's Thesis, Chengdu University of Technology, Chengdu, China, 2019. (In Chinese)
37. Zhao, Q. Late Cainozoic ostracod faunas and paleoenvironmental changes at ODP Site 1148, South China Sea. *Mar. Micropaleontol.* **2005**, *54*, 27–47. [CrossRef]
38. Wang, P.X.; Jiang, Z.M.; Zhao, Q.H.; Li, Q.Y.; Wang, R.J. Deep-sea evidence for the evolution and monsoon history of the South China Sea. *Chin. Sci. Bull.* **2003**, *48*, 2228–2239.
39. Xu, S.M.; Wu, P.; Zhang, W.; Zhang, H.Y.; Liu, Z.; Dai, L.M.; Li, J.W.; Li, L.B. Changes of paleocoastline in key geological periods in the South China Sea. *Mar. Geol. Quat. Geol.* **2013**, *33*, 1–10. (In Chinese)
40. Zhang, G.C. Theory of deepwater hydrocarbon accumulation controlled by progressive tectonic cycles of the marginal sea in the South China Sea. *Acta Pet. Sin.* **2023**, *44*, 569–582. (In Chinese)
41. Gao, Y.D.; Xiang, X.H.; Zhang, X.T. Cenozoic sedimentary evolution and its geological significance for hydrocarbon exploration in the northern South China Sea. *Nat. Gas Geosci.* **2021**, *32*, 645–656. (In Chinese)
42. Allen, P.A.; Allen, J.R. *Basin Analysis Principle and Application*; Blackwell Scientific Publications: Oxford, UK, 1990.
43. Yang, Q.; Qi, J.F. Method of delaminated decompaction correction. *Pet. Geol. Exp.* **2003**, *25*, 206–210. (In Chinese)
44. Wang, Y.L. Genesis of the glauconites in the Miocene Zhujiang Formation, Baiyun Sag, Pearl River Mouth Basin. Master's Thesis, Chengdu University of Technology, Chengdu, China, 2017. (In Chinese)
45. Zhang, Z.K.; Xie, L.; Zhang, Y.F.; Xu, J.; Li, S.H.; Wang, Y. Sedimentary records of the Mis 3 transgression event in the north Jiangsu Plain, China. *Quat. Sci.* **2010**, *30*, 883–891. (In Chinese)
46. Yao, W.J.; Liang, X.J.; Zhang, Y.Y. Geochemical characteristics of Quaternary sediments of typical borehole XJ01 in ancient Yellow River Delta. *Miner. Explor.* **2024**, *15*, 938–945. (In Chinese)
47. Jones, B.; Mamming, D.A.C. Comparison of geochemical indices used for the interpretation of depositional environments in ancient mudstones. *Chem. Geol.* **1994**, *111*, 112–129. [CrossRef]
48. Wang, Y.Y.; Guo, W.Y.; Zhang, G.D. Application of some geochemical indicators in determining of sedimentary environment of the Paleogene Funing Group, Jinhu Depression, Jiangsu Province. *J. Tongji Univ.* **1979**, *7*, 51–60. (In Chinese)
49. Sun, L.G.; Xie, Z.Q.; Zhao, J.L. The characteristics of Sr/Ba and B/Ga ratios in lake sediments on the Ardley Peninsula, Maritime Antarctic. *Mar. Geol. Quat. Geol.* **2000**, *20*, 43–46. (In Chinese)
50. Kim, J.; Kimura, Y.; Puchala, B. Dissolution enables dolomite crystal growth near ambient conditions. *Science* **2023**, *382*, 915–920. [CrossRef]
51. Zhang, Y.F.; Ma, Y.F.; Yao, Q.Z.; Qian, F.J.; Wang, Y.H.; Li, H.; Zhou, G.T. "Dolomite Problem"and Experimental Studies of Dolomite Formation. *Geol. J. China Univ.* **2015**, *21*, 395–406. (In Chinese)
52. Yang, M.L.; Liu, C.H.; Yang, W.Q.; Zhu, D.C.; Yu, Y.M.; Chen, F.Z.; Zou, H.Y. Characteristics and genesis of thick layer dolomites in the Lower Cambrian Xixiangchi Group, eastern Sichuan Basin. *Fault-Block Oil Gas Field* **2024**, *31*, 599–610. (In Chinese)
53. Qiang, Z.T. *Carbonate Reservoir Geology*; Press of the University of Petroleum: Dongying, China, 1998. (In Chinese)

54. Ren, Y.; Zhong, D.K.; Gao, C.L.; Yang, X.Q.; Xie, R.; Li, Z.P.; Deng, M.X.; Zhou, Y.C. Geochemical characteristics, genesis and hydrocarbon significance of dolomite in the Cambrian Longwangmiao Formation, eastern Sicuhan Basin. *Acta Petrol. Sin.* **2016**, *37*, 1102–1115. (In Chinese)
55. Zhou, Y.; Yang, F.L.; Ji, Y.L.; Zhou, X.F.; Zhang, C.H. Characteristics and controlling factors of dolomite karst reservoirs of the Sinian Dengying Formation, central Sichuan Basin, southwestern China. *Precambrian Res.* **2020**, *343*, 105708. [CrossRef]
56. Keith, M.L.; Weber, J.N. Carbon and oxygen isotopic composition of selected limestones and fossils. *Geochim. Cosmochim. Acta* **1964**, *28*, 1787–1816. [CrossRef]
57. Irwin, H.; Curtis, C.; Coleman, M. Isotopic evidence for source of diagenetic carbonates formed during burial of organic-rich sediments. *Nature* **1977**, *269*, 209–213. [CrossRef]
58. Zhang, X.L. Relationship between carbon and oxygen stable isotope in carbonate rocks and paleosalinity and paleotemperature of seawater. *Acta Sedimentol. Sin.* **1985**, *3*, 17–30. (In Chinese)
59. Huang, S.J.; Wu, W.H.; Liu, J.; Shen, L.C.; Huang, C.G. Generation of secondary porosity by meteoric water during time of subaerial exposure: An example from Yanchang Formation Sandstone of Triassic of Ordos Basin. *Earth Sci.* **2003**, *28*, 419–424. (In Chinese)
60. Yang, J.L. Characteristics and diagenetic significance of carbon and oxygen isotopes in the authigenic dolomites of lacustrine carbonate rocks—A case study of the Paleogene Shahejie Formation of the Shijiutuo Uplift in Bohai Sea. *Adv. Geosci.* **2017**, *7*, 847–855. (In Chinese) [CrossRef]
61. Tian, Y.M.; Shi, Z.J.; Li, T.Y.; Liang, X.W.; Xin, H.G.; Wu, X.M.; Gao, X. Characteristics and origin of the carbonate cement of Chang 8 member in Jiyuan area, Ordos Basin. *J. Xi'an Shiyou Univ. (Nat. Sci. Ed.)* **2011**, *26*, 26–31. (In Chinese)
62. Meshri, I.D.; Gautier, D.L. *On the Reactivity of Carbonic and Organic Acids and Generation of Secondary Porosity*; SEPM Society for Sedimentary Geology: Claremore, OK, USA, 1985; pp. 123–128.
63. Xu, B.M.; Lu, B. Study on carbonate cements in siliceous clastic rocks and their controlling effect on reservoirs. *Acta Sedimentol. Sin.* **1994**, *12*, 56–66. (In Chinese)
64. Lu, Y.S.; Hu, Y.; Hou, Y.D.; Sun, J.F.; He, W.X.; Gao, X.Y.; Si, J.; Song, W.X. Geochemical characteristics of trace elements in Yanghugou formation in the western margin of Ordos Basin and their implications for the sedimentary environment. *Sci. Technol. Eng.* **2021**, *21*, 11999–12009. (In Chinese)
65. Yang, Z.Y.; Sheng, W.Z.; Zheng, L.D. Elements and isotopic geochemistry of Guadalupian-Lopingian boundary profile at the Penglaitan section of Laibin, Guangxi Province, and its Geological implications. *Acta Geol. Sin.* **2009**, *83*, 1–15. (In Chinese)
66. Nan, J.Y.; Ye, J.L.; Wang, Z.M.; Zhou, D.Q. Geochemical study of Permian-Triassic paleoclimate and paleo-marine environment in Guizhou. *Acta Mineral. Sin.* **1998**, *18*, 239–249. (In Chinese)
67. Downey, M.W. Evaluating seals for hydrocarbon accumulations. *AAPG Bull.* **1984**, *68*, 1752–1763. [CrossRef]
68. Watts, N.L. Theoretical aspects of cap-rock and fault seals for single-and two-phase hydrocarbon columns. *Mar. Pet. Geol.* **1987**, *4*, 274–307. [CrossRef]
69. Fu, X.F.; Wu, T.; Lv, Y.F.; Liu, S.B.; Tian, H.; Lu, M.X. Research status and development trend of the reservoir caprock sealing properties. *Oil Gas Geol.* **2018**, *39*, 454–471. (In Chinese)
70. Zhang, W.D. Caprock Sealing Quantitative Evaluation of Low Abundance of Gas Accumulation. Master's Thesis, Northeast Petroleum University, Daqing, China, 2013. (In Chinese)